BARIUM BASED HALIDE SCINTILLATOR CERAMICS FOR GAMMA RAY DETECTION

by

WILLIAM TAYLOR SHOULDERS
B.S. Ceramic and Materials Engineering, Clemson University, 2011

A thesis submitted in partial fulfillment of the requirements
for the degree of Master of Science
in the Department of Mechanical, Materials and Aerospace Engineering
in the College of Engineering and Computer Science
at the University of Central Florida
Orlando, Florida

Summer Term
2013

Major Professor: Romain Gaume

ABSTRACT

As our understanding of ceramic processing methods for the purpose of fabricating polycrystalline optical materials has increased over the past few decades, the race is on to bring ceramic technology to markets where single crystalline materials have traditionally been used. One such market is scintillators. This Master's thesis focuses specifically on a class of materials attractive for use as gamma-ray scintillators. These barium based halides can potentially be utilized in applications ranging from ionizing radiation detection in the field to high-energy physics experimentation. Barium bromide iodide and barium chloride single crystals have already showed high light yield, fast scintillation decay, and high energy resolution, all desirable properties for a scintillator. This work attempts to show the likelihood of moving towards polycrystalline scintillators to take advantage of the lower processing temperature, higher manufacturing output, and overall reduced cost. The experiments begin with identifying appropriate sintering conditions for hot pressed ceramics of BaBrI and $BaCl_2$. Possible sources of optical loss in the first phase of hot pressed samples are investigated using a wide range of characterization tools. Preliminary luminescence and scintillation measurements are reported for a translucent sample of BaBrI. Recommendations are made to move toward highly transparent ceramics with scintillation properties approaching those measured in single crystal samples.

ACKNOWLEDGEMENTS

During my first year as a graduate student at UCF I hit a few speed bumps. I am thrilled to have progressed through four semesters of course work and research to the point where I am preparing my Master's thesis. For all their help in keeping me on track, I must first thank my research advisor, Romain Gaume, and my academic advisor, Kevin Coffey. I took a while to find my comfort here at UCF and now I have the students in CREOL and the Materials Science and Engineering departments to thank for making me feel like part of a family, a fun and quirky family at that.

Specific to the research contained in this document, I must first thank the other members of my research group: Dr. Samuel Paul David, Ali Jahromi, and the recent joinees, Sudeep Jung and Dr. Shi Chen. Romain, Samuel and I have worked closely together over the past year to setup our ceramics lab and begin work on halide ceramics. I must also thank them for allowing me to spend five months with collaborators at Oak Ridge National Lab while the work load at UCF was still very heavy. The team in Oak Ridge, Tennessee, who graciously allowed me to work alongside them for five months, consists of Dr. Lynn Boatner, Dr. John Neal, Joanne Ramey, and James Kolopus. Additional help on this project came from collaborators at Lawrence Berkley National Lab, Dr. Gregory Bizzari and Dr. Edith Bourret-Courchesne. Although I have never met them in person, they have provided me assistance in optical characterization of my samples.

I want to thank my fiancé, Heidi Lindler, for first agreeing to move down to Florida with me to pursue a higher degree and second for providing me with solace at home when work has often been hectic. Finally, our cat, Norris, has been a nice writing partner in the long nights I spent preparing this document.

TABLE OF CONTENTS

LIST OF FIGURES

LIST OF TABLES

1. INTRODUCTION

1.1 Project Motivation

This master's thesis is centered around the effort to develop new, high-performance scintillator materials specifically for use in gamma-ray detection. The compounds barium bromide iodide (BaBrI) and barium chloride ($BaCl_2$) have been chosen specifically for their high light yield in recent studies. These materials are projected to drive the improvement of detectors used for homeland security, high energy physics, deep well drilling, and space exploration. The Optical Ceramics Laboratory at UCF, under the direction of Dr. Romain Gaume, is currently involved in a multi-institutional effort with Oak Ridge National Laboratory (ORNL) and Lawrence Berkley National Laboratory (LBNL). As part of this partnership, I have conducted the research on barium bromide iodide at ORNL while research on $BaCl_2$ is largely confined to UCF. I routinely send samples of ceramics to LBNL for optical characterizations outside the abilities of UCF. This partnership has yielded a large amount of data in this first six months of work, however work by all parties continues beyond the period of the master's work.

The long-term goal of this work is to fabricate transparent ceramics of two potentially bright gamma ray scintillators, $BaCl_2$ and BaBrI, having similar scintillation performance to recent results on single crystal $BaCl_2$ and BaBrI. Due to the many factors playing into the performance of polycrystalline ceramics, it is not feasible to achieve excellent transparency and scintillation performance in the early stages of research. Therefore, the short-term goals of this project are as follows. First, I aim to create fully dense ceramics of $BaCl_2$ and BaBrI. Next, I seek to understand the phase composition and structure of the ceramics including analysis of impurity phases and defects. Expected hydrate, hydroxide, and oxide impurities lead to scattering and thus reduced optical quality. Additionally, deviation of the compounds from stoichiometry during processing may lead to the formation of charged defects (color centers). For the halide materials in focus, it is believed

that the achievement of high optical quality is strongly dependent on taking adequate measures to protect the reactive powders and samples from the ambient atmosphere during processing. This "hygroscopic" behavior is investigated.

The other parameters affecting the optical quality of ceramics include the volume fraction of pores, grain size, and grain orientation. In the context of the shorter term goals of this project, these parameters are considered secondary. The reason for this distinction between primary and secondary objectives is, first, a logical division of priorities to make the long-term goals manageable, and second, an attempt to understand the chemical limits to optical quality. Grain size, grain orientation, and porosity may require systematic studies in order to optimize their contribution to optical performance. However, if the chemistry of the compounds is not under control, the optical performance may never meet expectations. In this report, one will find these first steps towards achieving high performance scintillator ceramics of $BaCl_2$ and BaBrI.

1.2 Overview of Scintillators

The general textbook definition of 'scintillator' is a material that converts ionizing radiation into visible light. Scintillators are used in a broad range of applications including medical imaging, high energy physics and national defense. The basic setup of a scintillator-based detector includes the scintillation medium coupled to a photo-multiplier tube (PMT) or to a semiconductor optical sensing element. A series of electronics is used to amplify, shape, and convert the analog signal to the digital readout as seen in Figure 1. The energy of the light output from the scintillator is correlated to the energy of the ionizing radiation (x-rays, γ-rays, neutrons, etc.). Scintillation wavelength as well as brightness and decay speed vary widely between different scintillator materials, so scintillators are very application specific. Concepts related to scintillation are introduced below and discussed in greater detail the references texts by Knoll and Lecoq.[1,2]

The basic concepts behind scintillation involve the absorption of the ionizing radiation, the energy transfer to luminescent species and the optical emission processes.

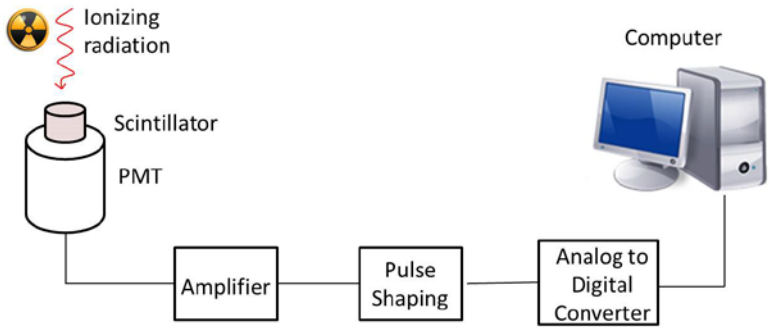

Figure 1: Schematic of a detector system used to characterize scintillator materials (i.e. pulse height spectrometry)

In scintillators, ionizing radiation is absorbed by the material through the photoelectric effect and results in the production of electrons and holes by a multiple elastic scattering process. The electrons and holes, eventually relax to the bottom of the conduction band and to the top of the valence band respectively, at which point they migrate and recombine radiatively. To enhance the radiative recombination of the charge carriers, the material is often doped with an "impurity" called activator, which traps the charges on energy levels lying within the band gap.

The terms "relaxation" and "migration" describe the basic ideas of how we are able to observe light emission from scintillators, but the energy decay processes are in fact very complex and highly material-specific. Ionizing radiation with energy much greater than the band gap (typically two to three times) creates electrons high in the conduction band and holes deep in the valence band. Those high energy electrons and holes get rid of their energy by elastic scattering and Auger processes until the excited electrons fall below the threshold energy ($\sim 2E_g$) for scattering. Electrons and holes lose further energy in the next step by a thermalization process in which phonons are emitted. The final steps of the energy decay are what really determine the performance of the scintillator. Electrons and holes in the thermal regime interact with the defect structures of the material or transfer to the material's luminescent centers, which ideally lead to the recombination of electron/hole pairs and the emission of photons. However, defects in the

material, namely impurities and color centers, may disrupt these ideal recombinations/emissions, a process which will be discussed later.

Table 1: Measured properties of two common commercial scintillator crystals taken from the scintillator property database[3]. *Light yield is measured under 137Cs excitation at 662 keV.

Property	Units	Tl:NaI	$Bi_4Ge_3O_{12}$ (BGO)
***Light Yield (Y)**	Photons/MeV	43,000	9,500
Energy Resolution (R)	%	7%	9%
Density ρ	g/cc	3.67	7.13
Decay Time(τ_{sc})	ns	230	340
Durability	N/A	Hygroscopic but easily encapsulated	Insensitive to atmosphere
Emission Wavelength	nm	415	480

The measurable physical properties related to scintillation performance are introduced in Table 1. The properties of thallium doped sodium iodide and bismuth germinate are presented to give an idea of the order of magnitude of the properties for typical commercial scintillators. The **light yield** of a scintillator is defined as the number of photons of light emitted per unit energy of ionizing radiation. The total light yield depends on the efficiencies of each of the charge creation-migration-recombination processes described above. The light yield is notably affected by non-radiative recombination (self-quenching), unwanted absorptions, and scattering. Fundamentally, light yield can be expressed as a product of three factors as in Equation 1.

$$Y = \alpha SQ \qquad (1)$$

where α is the photon to carrier conversion factor, S is the probability that carrier energy is transferred to an emitting center (intrinsic or dopant atom), and Q is the quantum yield of luminescent decay process. Assuming all transfer and conversion processes are perfectly efficient, the yield can be related to the number of electrons and holes in the material as proposed by Dorenbos.

$$n_{e/h} = \frac{E_\gamma}{\beta E_g} \qquad (2)$$

Thus, from Equation 2 the light yield is found to be inversely proportional to the electronic bandgap (E_g). The energy of the ionizing radiation is given by E_γ while β is a constant assumed to have an

approximate value of 2.5 MeV/ph[4]. Light yield is measured experimentally by the brightness of scintillation light produced from a scintillator excited by a monochromatic source of radiation. Because NaI is used as the industry standard for brightness, light yields for the BaBrI and $BaCl_2$ in this study are compared to NaI.

Energy resolution refers to the material's ability to distinguish between different energies of radiation. The energy resolution of a scintillator is primarily determined by photon statistics and therefore improved resolutions are obtained with high light yield materials. There is also an intrinsic component to the resolution which is related to the fact that the light yield is not a truly linear function of the incident energy, particularly at energies below 100 keV. This so-called non-proportionality of the response can be explained by the creation of electronic excitations including photoelectrons (photon absorbed, electron emitted), Compton electrons (incident photon "knocks loose" and electron and the two particles are scattered away at different angles), and Auger electrons (emitted due to the filling of an empty core atomic energy level)[5]. The line width of the photo-peak in the energy spectrum of a scintillator is determined by the relative numbers of these electronic excitations created by an incident photon. Finally, the electronic noise originating from the light detector (shot noise and Johnson noise) limit the overall resolution of the detector. Resolution is determined experimentally by the ratio of the brightness of the scintillator output versus its bandwidth for a monochromatic excitation source.

Stopping power can be described by the attenuation length of ionizing radiation in the material. A material should stop all incoming photons before they reach the PMT. The attenuation length (μ) is defined as the depth at which the intensity of the ionizing radiation has dropped to 1/e of the initial value. μ can be approximated with Equation 3 by taking into account the number of photoelectron and Compton scattering events.

$$\mu = \frac{m_f}{\rho(\sigma_c+\sigma_{pe})} \qquad (3)$$

In Equation 3, m_f is the formula mass, ρ is the mass density, and σ_c and σ_{pe} are Compton and photoelectric scattering cross-sections respectively. To calculate the intensity of the radiation at any depth within the material, Beer-Lambert's law is used, as shown in Equation 4.

$$I(x) = I_0 \exp(-x/\mu) \qquad (4)$$

Because σ_c and σ_{pe} can be difficult to approximate, often the material's density is the major factor considered in stopping power.

The **decay time** is the time elapsed from the first elastic interaction between the ionizing radiation and bound electrons to the sensing of a photon of light. As described above, decay takes place in multiple steps the decay times for which may vary over several orders of magnitude. A much slower decay component causing "afterglow" lasting seconds to hours after the initial collision of a high energy photon can also be present. Afterglow is caused by the trapping of electrons at lattice defects and contributes to higher background signals during measurements. In some applications, such as high counting rate or medical Positron Emission Tomography (PET), time resolution of the scintillator is important and afterglow is highly detrimental.

Finally, the **emission wavelength** of the scintillator should be well matched to the maximum efficiency of current PMT or semiconductor detectors, which is typically between 400nm and 500nm. The emission wavelength is fundamentally determined by the electronic band structure of the material and measured by a spectrophotometer.

1.3 Searching for New Scintillator Materials

A wide range of scintillator materials including inorganic bulk single-crystals, glasses, nanoparticles and organic polymers has been studied. Today, however, single crystals remain the sole class of scintillators capable of competing with semiconductors for high-energy gamma ray detection where high brightness and energy resolution are needed. Up until recently, the discovery of new scintillator materials was a very slow process. Simple models, for instance Equation 2, can predict the performance of a compound. Intuition and experience on the energy band structure

created by the addition of specific dopant ions can also be used. However, to properly test scintillation performance, crystals were grown by labor intensive techniques. In recent years, not only in the field of scintillator research but in many other fields as well, new materials have increasingly been identified by both rapid fabrication methods and high-throughput computer modeling[6].

Lawrence Berkley National Lab (LBNL) made significant progress with the former approach beginning in the late 1980s up to the current day. This approach and its findings are discussed in detail in the literature[7–9]. Other national labs in the United States have launched their scintillator research efforts to include specific classes of materials, including halides and garnets [10]. At LBNL, the first step for the rapid experimental method was the mining of crystal data from the National Institute of Standards and Technology (NIST) database, featuring hundreds of thousands of inorganic compounds from past scientific studies. Properties of interest in this data mining were favorable core-valence transitions (intrinsic scintillators), high density, absence of absorptive metals, and no intrinsic radioactivity. Once candidate materials were identified, polycrystalline samples were obtained by either searching material archives from previous studies or synthesizing new material. The rapid preparation and screening of 100s of viable scintillator compounds was initially reported in the early 2000s. Stoichiometric amounts of precursor powders from commercial vendors were batched and melted to form the compounds in accordance with available phase diagrams. Samples were then placed in special sample holders for analysis by large batch x-ray diffraction (16 sample automated measurement), x-ray excited luminescence (multiple sample turret), and a pulsed x-ray system used to estimate the decay time. From this study, a shorter list of promising scintillator materials was constructed. Research conducted on high purity crystals followed.

Even with the improved efficiency of rapid experimental screening techniques, the discovery of new materials by experimental methods alone is severely limited. Careful screening of

100 compounds, which has taken place over the past decade with the method described in the previous paragraph, only takes care of a small fraction of the known compounds. For this reason, modern approaches to problems in materials science include computational materials design. One computational method used effectively to screen scintillator materials, among other classes of materials (thermoelectrics, solar energy materials, etc.), is known as high throughput (HT) computational materials design. The HT approach uses a combination of data mining, quantum mechanics, and thermodynamics requiring lots of computing power[6,11,12].

First, the mining of data from the international crystal structure database (ICSD) narrows the field of potentially good scintillators to a manageable level, much like the first step of the experimental approach. Next, comprehensive models of electronic structure are used to predict scintillation behavior. Models have been shown to predict the band gap somewhat accurately, however estimation of light yield, resolution, and decay time is less trivial. Comparisons between the experimental and calculated light yield (Y) for the well-known scintillators NaI, BGO, and YAG shows an under-estimate in the calculations[11]. The most difficult parameter of the light yield calculation to predict is the carrier to photon conversion factor (α), which varies with temperature and between materials. Nevertheless, the purpose of developing these models is for the discovery of new materials, not predicting the absolute values of material properties. The HT computational methods have provided a good basis for more detailed experimental studies that take into account more practical aspects of materials selection such as the ability to synthesize the compounds in a laboratory.

1.4 Polycrystalline Ceramic Scintillators

In the materials science community, a ceramic is usually defined as a man-made inorganic, non-metallic polycrystalline material. An etched ceramic viewed under an optical microscope may have a grain structure similar to that shown in Figure 2. Because grains are most often oriented randomly, the mechanical and in our case optical properties encounter discontinuities at grain

boundaries. The wide use of translucent and transparent ceramics actually dates back to the 1960s, when translucent α-alumina was used in the bulbs of high pressure sodium vapor lamps[13]. Alumina has a hexagonal crystal structure(anisotropic), but still transparencies above 70% in the visible regime have been obtained due to low optical anisotropy.[14] Other uses for transparent ceramics include transparent body armor for military vehicles ($MgAl_2O_4$ spinel) and laser gain media (RE^{3+}:$Y_3Al_5O_{12}$ yttrium aluminum garnet). Single crystal scintillators like those mentioned above are currently the state of the art for high energy gamma ray detection. The search for new materials certainly begins with the identification of candidate compounds. However, the high throughput search methods preclude serious considerations about fabrication and thus the growing of single crystals versus the sintering of ceramics.

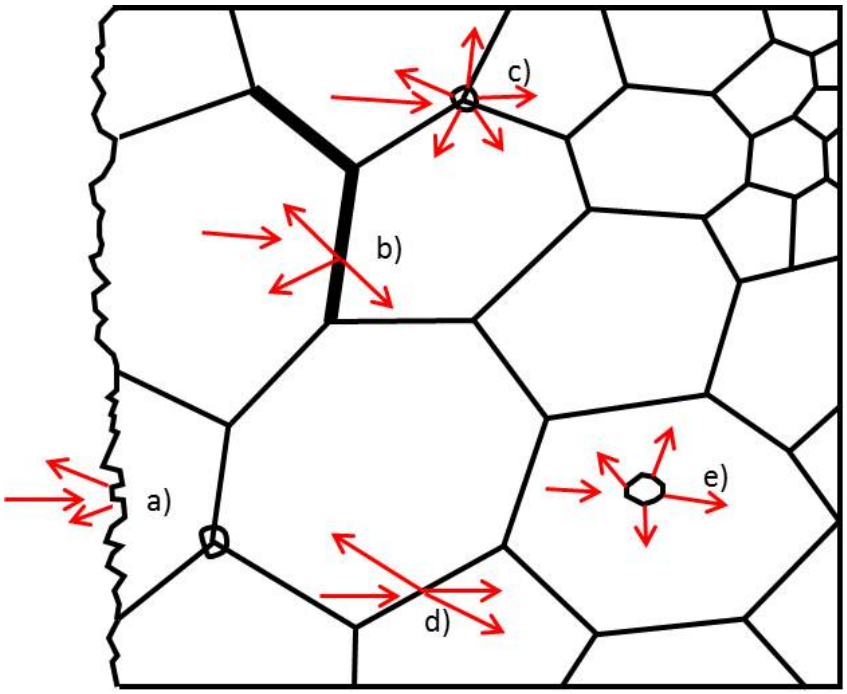

Figure 2: Sources of scattering in transparent ceramics include a) rough surfaces, b) 2nd phases at grain boundaries, c) porosity, d) birefringence at grain boundaries, and e) inclusions

There are several key limitations for available crystal growth methods.

1. Processing temperature
2. Processing time
3. Reactivity with ambient atmosphere, growing vessels
4. Cost of raw materials

The first two issues may be addressed by moving towards polycrystalline ceramic materials. The process of forming fully dense ceramics from powders, known as sintering, takes place below the melting temperature of a compound. Where crystal growth techniques, such as Bridgman-Stockbarger, may take weeks at the melting temperature to grow a crystal a few centimeters in length, most sintering techniques require only a matter of hours. Single crystals are also limited in geometry (especially diameter), while polycrystalline ceramics can be made available in larger and more complex geometries. One other notable advantage of ceramics over single crystals is increased control over dopant concentrations and profiles. This is extremely useful for tailoring the properties of solid state lasers, but also has implications for improved scintillator output. Besides differences related to processing, the resulting properties of ceramics are different than those of their single crystal counterparts. The presence of grain boundaries in ceramics improves their mechanical strength compared to crystals. Grain boundaries are also effective in altering other physical properties including thermal conductivity. With these advantages come additional challenges for achieving good optical quality in a ceramic versus a single crystal.

1.4.1 Sources of Optical Loss in Ceramics

The fabrication of polycrystalline ceramic scintillators also has its challenges. Most importantly, the transparency of a ceramic (and ultimately light output of the scintillator) is determined by the extent of scattering and absorption. The sources of scattering are represented in Figure 2. First of all, the anisotropy of the refractive index (birefringence) between neighboring grains in a polycrystalline ceramic leads to Fresnel losses. In this phenomenon, which follows

Snell's law, light refracts at the interface between two dissimilarly oriented grains. The angle of refraction depends on the direction of propagation of the light ray with respect to the crystalline orientation of the grains and to that of the grain boundary. This is quantified by the magnitude of the difference in the refractive index (Δn) for this orientation. Other sources of scattering may also exist. Incomplete densification of the ceramic results in residual porosity ($n_{pore} \approx 1$), which strongly scatters the scintillation light. Most optical materials have an index of refraction much higher than 1, so this usually has a much stronger effect than birefringence alone. For instance, at a wavelength of 550nm NaI has $n \approx 1.77$ and BGO has $n \approx 2.57$. Several other sources of scattering is shown in Figure 2. Basically any inhomogeneity in the refractive index will lead to scattering.

Optical absorptions can also lead to a decrease in transmission of a transparent ceramic sample. These absorptions come from heightened concentrations of chemical and structural defects[15,16]. The presence of charged defects, known as "farben centren" or color centers are frequently observed in the halide materials of interest in this study. The F-center, an electron trapped in an anion vacancy, is a common color center in halide materials. This trapped electron has its own characteristic resonance in the visible frequency range.[17,18] This is the simplest example of a color center, but many other types of charged defects can be formed.

1.4.2 Performance of Ceramic Scintillators

The challenges of absobers and scatterers have been largely overcome for a small set of scintillator ceramics. Table 2 compares the properties of polycrystalline ceramic scintillators to their single crystal counterparts. To date, ceramic scintillators often show poorer characteristics than their single crystal counterparts due to the greater challenge of eliminating all sources of optical loss.

Table 2: A comparison of single crystalline and ceramic scintillator properties. References are given next to values. * All energy resolution and light yield data points were measured under ^{137}Cs excitation, 662keV.

Material	LSO: Ce crystal	LSO: Ce ceramic	$LaBr_3$: 0.5%Ce crystal	$LaBr_3$: 1%Ce ceramic	BGO crystal	BGO ceramic
Refractive index	biaxial	biaxial	uniaxial	uniaxial	isotropic	isotropic
Light Yield (Ph/MeV)	33000[19]	28000[19]	75000[20]	42000[19]	10600 [21]	<10000[22]
Energy Resolution (%)*	9[23]	18[23]	2.9[24]	>3	9.05[21]	
Decay Time (ns)	42[19]	32.8[19]	30[24]		300[25]	
Emission Wavelength (nm)	405[19]	420[19]	356; 387[24]		485[25]	500[22]

1.5 Barium Halide Based Scintillators

One takeaway from the recent efforts to survey broad composition spaces for potential scintillator materials is the attractiveness of the alkaline-earth halide salts. In this body of work, I focus specifically on the barium halides. These compounds possess simple crystal structures with predictable scintillation decay mechanisms. Additionally, their lattices are accommodating to the size and charge of common rare-earth elements used as activators. From the processing standpoint (covered in more detail in chapter 2), the barium halides are readily available at relatively low raw materials costs, have relatively low melting temperatures, and exhibit lower activities with air than some other promising metal halide scintillator materials such as SrI_2 and $LaBr_3$. The following discussion covers the work on alkaline earth halides in the past fifty years leading up to the current interest in barium based halides.

Publications on strontium iodide have been frequent over the past decade due to its high light yield and the proportionality of its response. As is the case for many of the binary alkaline earth halides, researchers have found a renewed interest over the past two decades due to improvements in the crystal growth techniques and more recently ceramic processing. Europium

doped SrI_2 crystals are now commercially viable gamma ray scintillators[26]. Studies on ceramic SrI_2 have revealed that its high reactivity with the ambient atmosphere (H_2O and O_2) is the largest obstacle in producing samples with adequate transparency[27]. To maintain a clean working environment throughout the entire ceramic fabrication process has been a major challenge. Nonetheless, SrI_2 ceramic scintillators are still an active area of research. In this work, experimental data for SrI_2 is often used as a comparison for the $BaCl_2$ and BaBrI.

Other alkaline earth halides have also been studied over the years. Binary compounds are naturally the easiest to study from a chemical and structural standpoint. The availability of experimental data from as early as the 1930s (when scintillator materials were not at the forefront of scientific research) is also helpful in surveying their potential as scintillators. Calcium compounds, although the least dense of the alkaline earth halides discussed here, have found their share of applications. Calcium fluoride has been used as an x-ray detector since the middle of the 20th century and also as a tritium detector[28]. However, the stopping power and brightness of CaF_2 are not sufficient for gamma ray detection applications of interest in this work. One can still learn from the tremendous progress made on this material. Scientists in Russia have fabricated highly transparent CaF_2 nano-ceramics[29]. Grain sizes on the order of tens of nanometers can lead to effective optical isotropy for materials possessing non-cubic crystal structures. The method of nano-structuring as well as other methods useful in working towards transparent non-cubic materials, such as grain texturing, will be discussed later in the context of barium chloride ceramics.

Another binary compound, barium fluoride, was first tested as a scintillator in the 1980s. In its pure form, BaF_2 has three overlapping emission bands, which can be a severe limitation to the resolution. This is compensated by the fast decay. The ultra-fast core-valence luminescence mechanism (typically much faster than decay in doped scintillators) is only possible in a limited number of ions, Ba^{2+}, Rb^{+}, Cs^{+}, and K^{+} and happens to occur most rapidly in BaF_2[30]. The band accounting for 80% of the light output has a very slow decay time (>600ns), however the other

emission band corresponds to a very fast decay component (<1ns), making this material attractive for high counting rate applications[31]. The slower decay components may be suppressed by adding activators, but not without sacrificing scintillation performance in other regards[32]. BaF_2 has its niche in high counting rate applications not requiring high light yield. It is currently available from industrial crystal growers mainly for use as a detector in positron emission tomography (PET scans).

The other binary barium halides in their undoped, cerium doped, and europium doped forms have been studied extensively[33,34]. Ce: $BaBr_2$ and Eu: $BaCl_2$ have yielded promising experimental results, while barium iodide shows very poor light yield. However, these materials have yet to exceed the performance of current state of the art single crystal scintillators (i.e. NaI). Barium chloride ceramics are a major component of this study, so this material will be treated in more detail in the next section. The mixed halides have also been investigated. The halofluorides (Ba*X*F, where *X* is Cl, Br, or I) display poor scintillation properties due to the trapping of electrons at intrinsic defect sites[35]. The reason for failure of these compounds is speculated to come from the complexity of the structure formed from the combination of fluoride and 'X' compounds. BaF_2 is cubic, while the other barium halides adopt an orthorhombic crystal structure. The conditions for the formation of an extended solid solution are not favorable and a high concentration of defects is likely. Generally, disordered and complex crystal structures are undesirable for scintillator applications for this reason.

In conclusion, many alkaline earth halide materials have been investigated for their optical and scintillation properties over the years. The two materials at the focus of this work have not been treated as extensively as many of those mentioned above. Both barium bromide iodide and barium chloride have narrow bandgaps (5.78eV and 4.12eV respectively), meaning the theoretical limits to their light yields according to Equation 2 are roughly 46,000 ph/MeV and 64,000 ph/MeV respectively. The Eu^{2+} dopant substitutes directly for the 2+ charged cations in the crystal structure

and the energy levels of Eu^{2+} fall within the bandgap of both materials. This potential for high light yield scintillation has been identified by a combination of computer and experimental results.

1.5.1 Barium Chloride

Barium Chloride has garnered interest at a gamma ray scintillator in recent years. It adopts an orthorhombic $PbCl_2$-type crystal structure (Space group 62) from room temperature all the way up to 925°C, at which point it transforms into a cubic phase until the melting point of 962°C. Even though the structure is orthorhombic (a~7.865Å, b~4.731Å, c~9.421Å), the optical symmetry is nearly biaxial with a $\Delta n \sim 0.012$ (n_a~1.7302, n_b~1.7361, n_c~1.7420)[36]. The limit on optical quality of $BaCl_2$ ceramics is assumed to come predominantly from the birefringence at grain boundaries. The table below shows experimentally measured light yield, decay time, afterglow, and energy resolution for undoped, cerium doped, and europium doped $BaCl_2$.

The x-ray luminescence (XL) spectrum of pure $BaCl_2$ shows three overlapping peaks, two of which have been attributed to the afterglow in the sample[33]. The broad and overlapping XL peaks correspond to a lower energy resolution. By contrast, the europium doped samples display only 2 overlapping peaks, one of which (406nm) originates from a 5d-4f transition in Eu^{2+}. Furthermore, the light yield is over 15% higher than NaI.

Table 3: Scintillation performance of $BaCl_2$ crystals. All light yield measurements were done with a 10μs pulse shaping time. The afterglow is measured at the emission wavelength of the major fast decay components of each sample.

Material	$BaCl_2$, [29]	5% Eu^{2+}: $BaCl_2$ [29]	0.1 %Eu^{2+}: $BaCl_2$ [29]	[34]0.1% Ce^{3+}: $BaCl_2$ [30]	[34]1% Ce^{3+},K^+: $BaCl_2$ [30]
Light Yield (phonons/MeV)	1700±150 (at 10 μs)	52,000 (at 10μs)	19400±1950 (at 10 μs)	3100±300 (at 10 μs)	5300±500 (at 10 μs)
Decay Time (ns)	980±100 (100%)	25ns (15%) 138ns (21%) 642ns (61%)	390±40 (100%)	14±1 (10%) 90±9 (40%) 1400±140 (50%)	7±1 (6%) 190 (11%) 1500±150 (80%)
XL to afterglow ratio (%)	25% at 475nm	-	0.2% at 402nm	8% at 370nm	35% at 370
Energy Resolution (%)	17.4±1.7	3.5±0.3	8.8±0.9	14±1.4	16.2±1.5

When activating $BaCl_2$ with Ce^{3+}, the XL spectrum shows two overlapping peaks representative of the ground state splitting of the 4f energy level in cerium as well as two extra peaks of lower intensity[34]. Figure 3 shows the energy level diagrams for Ce^{3+}. The decay in Ce^{3+} takes place from the $5d_2$ to either of the 4f levels and yields a blue emission. The decay in Eu^{2+} occurs from an energy within the continuum of the 4f and 5d bands resulting from orbital mixing with the ligands. One study of polycrystalline Ce:$BaCl_2$ showed the presence of the Ce^{3+} doublet in the luminescence spectrum upon optical excitation, but a single broad peak upon x-ray excitation, which may be a consequence of radiation damage. Co-doping of Ce^{3+} with K^+ suppresses the extra luminescence peaks but the Ce^{3+} doublet remains, ultimately leading to poorer performance compared to the europium doped material.

In addition to testing the performance of Ce^{3+} as an activator, recent studies have found that cerium doped in excess of 5 mol% stabilizes the cubic phase of $BaCl_2$ at room temperature. Coarse grained ceramics quenched from a melt of anhydrous starting material held above 925 °C display qualitatively good transparency and show minor differences in performance compared to their single crystalline counterparts [37].

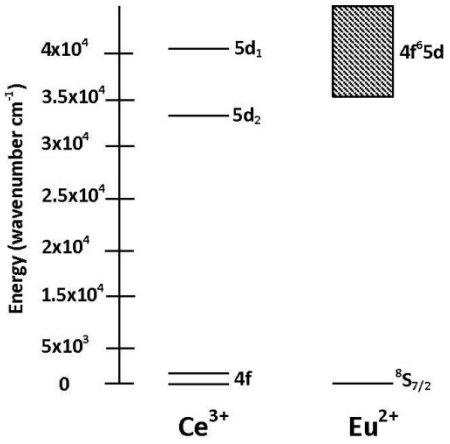

Figure 3: Energy level diagram for 2 common activators used in scintillator materials. The absolute energies of the levels will fall within the band gap of the material and will also be dependent on the crystal field.

The evaluation of scintillation performance in these 5% Ce^{3+} doped $BaCl_2$ ceramics showed a light yield of 7,200 ph/MeV, resolution of 23% and fast initial decay component of 50ns. Yttrium, lutetium, samarium, gadolinium, and lanthanum cations have also been tested to stabilize the cubic phase in $BaCl_2$ at room temperature[37,38]. Figure 4 shows a phase diagram for a pseudo-binary system which is not suitable for stabilizing the cubic phase. The region of solid solution between 301°C and 600°C is an indicator that the two cations can form a solid solution of the hexagonal phase. However, a high temperature solid solution of cubic barium chloride and cubic CsCl is required for a quenched sample to retain the cubic structure at room temperature. This is not observed in the phase diagram.

A study of the $BaCl_2$ –$LaCl_3$ phase diagram shows some uncertainty in the $BaCl_2$ –rich phases due to a lack of data points. Studies by Edgar, et. al. suggest that a solid solution between these two compounds should appear near the melting point and moderate cooling rates are successful in retaining that cubic solid solution at room temperature.

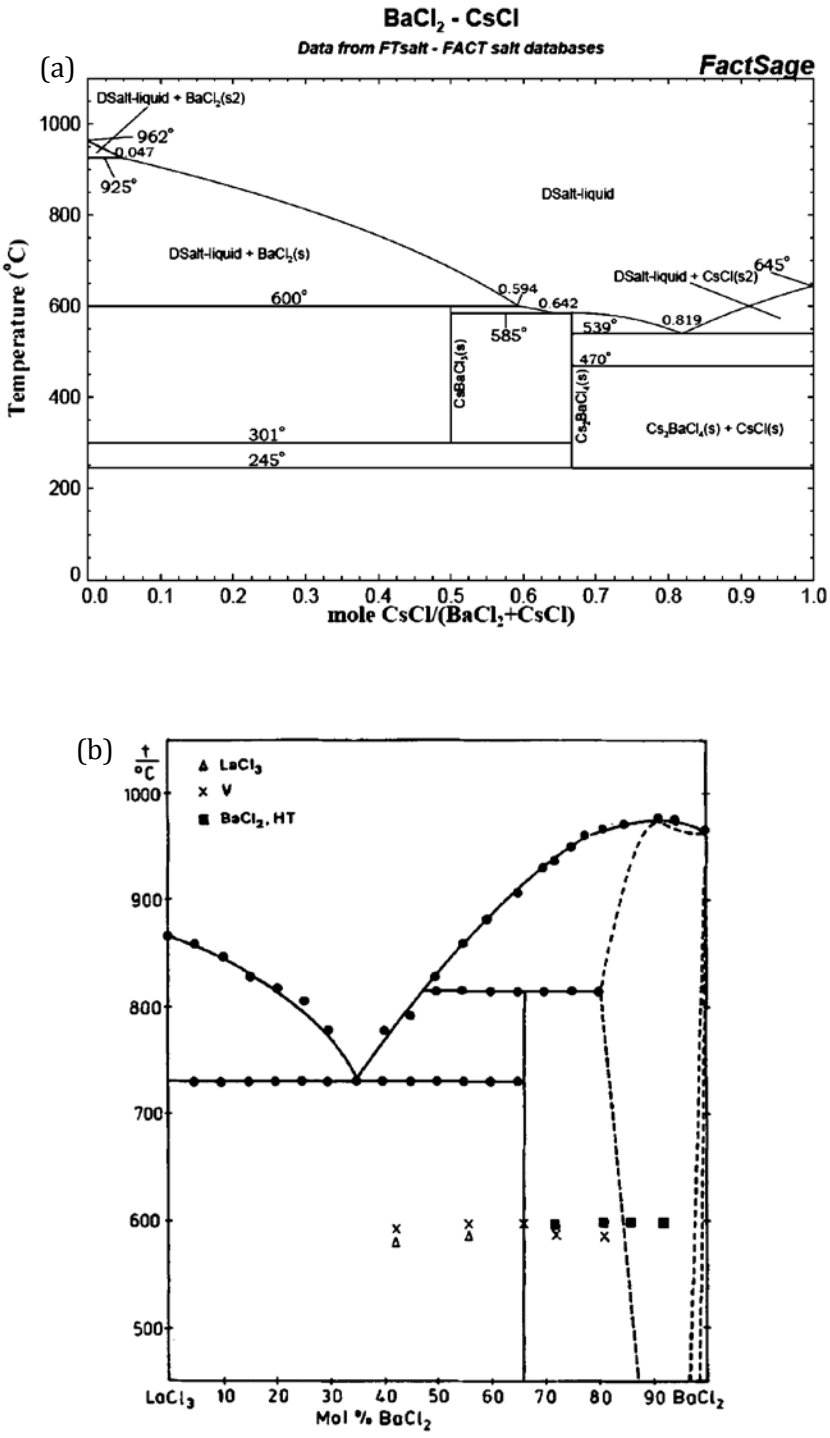

Figure 4: (a) $BaCl_2$ – $LaCl_3$ phase diagram from FACT database showing the high temperature cubic phase and (b) $BaCl_2$ – $LaCl_3$ phase diagram developed by Blachnik showing high temperature solid solution[39,40].

These literature results make sense in the light of the similarity of ionic size of Ba^{2+} and La^{3+}, assuming 8-coordinated barium and 9-coordinated lanthanum in the cubic structure[41]. The cubic

phase was achieved in both 11% Gd^{3+}:$BaCl_2$ and Gd^{3+}, Ce^{2+} co-doped $BaCl_2$. For the lanthanum stabilized material, the luminescence is suspected to originate from the excitement of chlorine interstitials, trapping of electrons on lanthanum ions, and the migration of electrons to europium centers. Thus the chemical stabilization of cubic $BaCl_2$ has its trade-offs with scintillation performance, and is not of interest at the moment.

1.5.2 Barium Bromide Iodide

Barium bromide iodide (BBI) is a more recently discovered scintillator material being grown at LBNL and Radiation Monitoring Devices, Inc[33,42]. BBI melts at 850 °C and adopts $PbCl_2$ structure just like $BaCl_2$. Due to the limited amount of experimental data available on this material, simulations using density functional theory (DFT) have predicted additional properties[43]. The band gap of BaBrI, calculated by three different methods, is found to be 5.78±0.67eV on average. The average refractive index deviation (Δn) between the three principle axes for BBI was found to be approximately 0.02. The magnitude of this refractive index variation is rather large, causing transmission to drop rapidly in a sample having an average grain size on the order of hundreds of nanometers. This calculation for scattering by birefringence is based on Rayleigh-Gans-Debye theory. Assuming random orientation of grains, uniform grain size distribution, no pores, no inclusions, and no secondary phases, the relative inline transmittance is approximated by Equation 5, originally presented by Apetz[44].

$$RIT = (1 - R_s)\exp(\frac{3\pi^2 r(\Delta n)^2 d}{\lambda_0^2}) \quad (5)$$

R_s is a parameter based on the difference in refractive index between 2 crystallographic directions given by Equation 6.

$$R_s = \frac{(n_1 - n_2)^2}{(n_1 + n_2)^2} \quad (6)$$

For the purpose of this approximation, n_1 is taken to be the average refractive index of the material and n_2 the average n plus the average deviation of n between the 3 principle axes. In Equation 5, r is

the grain size, d is the thickness of the sample and λ_0 is the wavelength for which transmittance is measured. A plot showing transmittance versus grain size for a 2mm thick sample of BaBrI at 435nm is given in Figure 5.

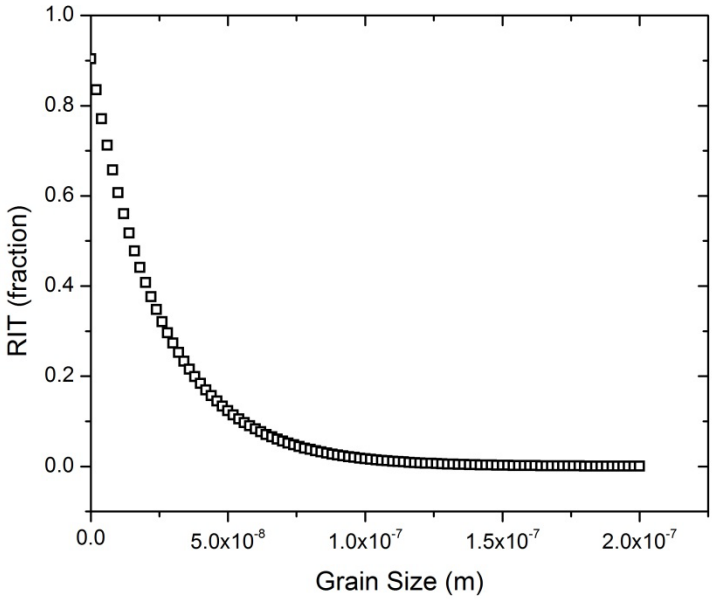

Figure 5: Apetz's model for scattering due to birefringence in a ceramic having Δn=0.02, thickness=2mm, n_{avg}=1.90. This relative transmittance curve is calculated for a wavelength of 435nm.

The model predicts that a grain size on the order of nanometers will be necessary to achieve good transparency in a 2mm thick sample of BaBrI. It is important to recognize that this model predicts inline transmittance, which is a much more stringent measure of transparency compared to the industry standard practice of showing pictures of thin ceramics placed on top of text. A significant number of scattering events may occur without adversely affecting the ability to read text through a ceramic. Scattering is not necessarily detrimental to scintillator performance as long as the scintillator is packaged appropriately with reflecting material along its edges such that light eventually makes its way to the photo-detector. If birefringence does surmount to a major obstacle for adequate transparency, methods of preferentially orienting grains or nano-sizing grains will need to be investigated.

The two samples summarized in Table 4 were fabricated and tested by the same research group at LBNL. The sample from reference 40 shows one of the highest light yields of any scintillator measured to date (over 2x NaI). The light yield is also higher than that estimated by Equation 2.

Table 4: Measured scintillation properties in 2 different BaBrI single crystal samples. Light yield is measured under 137Cs excitation. Optical excitation for decay measurements in the first sample was done at 400nm. The 2 component decay in the second sample was measured under x-ray excitation.

Material	BaBrI: 8% Eu^{2+}, [45]	BaBrI: 8% Eu^{2+}, [38]
Light yield	91,100	81,100±3000
Energy resolution (%)	3.4	4.8
Decay Time (ns)	418±21	297 (23%) 482 (77%)

The authors have suggested that the improvement in light yield and energy resolution over their two publications can be attributed to the refinement of the crystal growth method for BaBrI. The crystals are typically grown by the Bridgman method with the biggest obstacles to high quality being the material's high reactivity with water and the organic impurities in the commercial starting powders (discussed later). The next chapter focuses on the experimental techniques used in the fabrication and characterization of BaBrI and $BaCl_2$ ceramics.

2. EXPERIMENTAL TECHNIQUES

2.1 Overview of Experiments

This project is centered on the fabrication of barium based halide ceramics and their subsequent characterization. Starting materials are either single crystals grown by the Bridgman-Stockbarger technique, anhydrous commercial powders, or di-hydrate commercial powders. Powders are hot pressed into ceramics having typical densities of 98% ± 2% relative to the theoretical density. Hot pressed ceramics are subsequently hot isostatically pressed (HIPed) to collapse any remaining closed porosity. Additional post-treatment of samples by annealing is sometimes necessary to reverse chemical reactions that result in coloration of the samples. Basic optical sample preparation by grinding and polishing parallel surfaces is necessary for most characterization techniques.

Many common structural and optical characterization tools have been used for this project. The structural characterization techniques include x-ray diffraction (XRD), micro-Raman spectroscopy, and scanning electron microscopy. Thermogravimetric analysis (TGA) is also used to examine the mass lost from the starting powders upon heating. The optical transmission of the samples is measured by ultraviolet-visible spectrophotometry. The subset of scintillation characterization techniques includes x-ray excited luminescence (XRL) to measure a sample's emission under low energy (1-100keV) excitation, decay time measurement using a pulsed x-ray source, and finally light yield and resolution measurement using pulse height spectrometry.

2.2 Sample Preparation

2.2.1 Preparation of Precursor Powders

The easiest route toward transparent ceramics of barium based halides is expected to be through the hot pressing of crushed powders derived from highly pure single crystals. Crystals of BaBrI doped with between 3% and 6% by weight of $EuCl_2$ are grown by the Bridgman method at

ORNL and LBNL. Anhydrous powders of $BaBr_2$, BaI_2, and EuI_2 each having purities of at least 99.99% are batched in stoichiometric amounts in an argon filled glove box maintained at <100ppm H_2O and <50ppm O_2. The batch is then sealed in a quartz ampoule and reacted under vacuum to form the BaBrI compound at 850°C. The ORNL process for purifying BaBrI is described in Figure 6. The process uses a glass filter with a 100µm pore size, which lets the molten halide phase through and leaves behind a black organic residue.

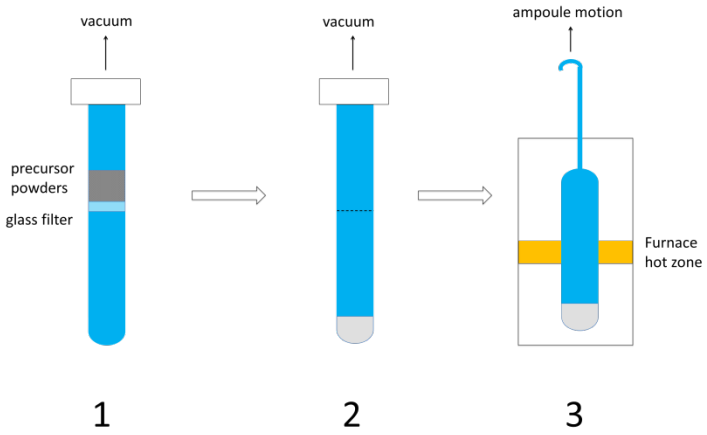

Figure 6: Schematic of the crystal growth process I used at ORNL 1) melting mixed precursor powders through a quartz filter under vacuum, 2) sealing the quartz ampoule, and 3) growing a crystal by the Bridgman method.

After purification and the formation of the BaBrI phase above 850°C, the quartz tube is sealed with a hydrogen torch below the filter and attached to a quartz rod for suspension in the vertical Bridgman furnace. In a typical Bridgman crystal growth, the ampoule is lowered through the melting zone at a rate of approximately 0.04mm/h, meaning a single pass through the hot zone takes approximately three weeks to grow a crystal several inches in length. Some systems may also rotate the ampoule while pulling to homogenize the melted region. The Bridgman technique also acts to purify the material. This is similar to the method of zone refining, as an ampoule is pulled slowly through the hot-zone of a furnace, which has been set at the melting temperature of the material. The difference in solubility of impurities in the two phases at the solid-liquid interface will cause the impurities to either accumulate in the melt (higher solubility in melt, i.e. segregation

coefficient k<1) or crystallize at the edge of the melt zone (lower solubility in the melt, i.e. segregation coefficient k>1)[46]. In practice, in the semi-conductor industry, hundreds of cycles are used to achieve high purity crystals. Synthesized crystals possess multiple grains in some cases but exhibited high clarity and no visible coloration. Impurities are concentrated at one end of the ampoule. An example of a colorless crystal grown at LBNL is shown in Figure 7.

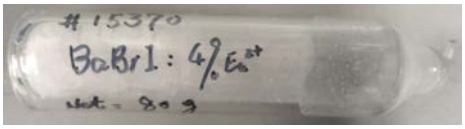

Figure 7: Colorless Eu:BaBrI crystal grown at LBNL

Thus far in this work, a more practical route has been adopted for the preparation of $BaCl_2$. Commercial powders of anhydrous $BaCl_2$ and the di-hydrate ($BaCl_2$-$2H_2O$) are directly filled into the hot pressing die without purification. This disregards the removal of any organic residues at the moment, but $BaCl_2$ powder preparation will employ a filtration method such as that used at ORNL in the future. The reason for also disregarding the impurities due to water (hydrate) is the observation in literature that $BaCl_2$ is one of few compounds whose hydration is completely reversible[47]. Thus, if anhydrous starting powder is exposed to air, it should still dehydrate completely before sintering begins to occur. The same holds true if the starting powder is a di-hydrate and furthermore the di-hydrate is stable and easier to handle in air. The removal of two molecules of water from each molecule of $BaCl_2$ in the confined space of a hot press die under one atmosphere of flowing argon may prove to be too difficult, however the pressing of di-hydrate powders is a very easy experiment to try.

For this study, regardless of the powder preparation method, the material is crushed in small batches (~10g) with a mortar and pestle (inside the glove box for $BaCl_2$) to achieve a particle size on the order of a few micrometers. Anhydrous powders are ground just before loading into a die to avoid excessive moisture absorption.

2.2.2 Hot Pressing

Hot pressing is carried out in one of two systems: a carbon-free press built by the ORNL team and a commercial press from Thermal Technology, Inc. at UCF.

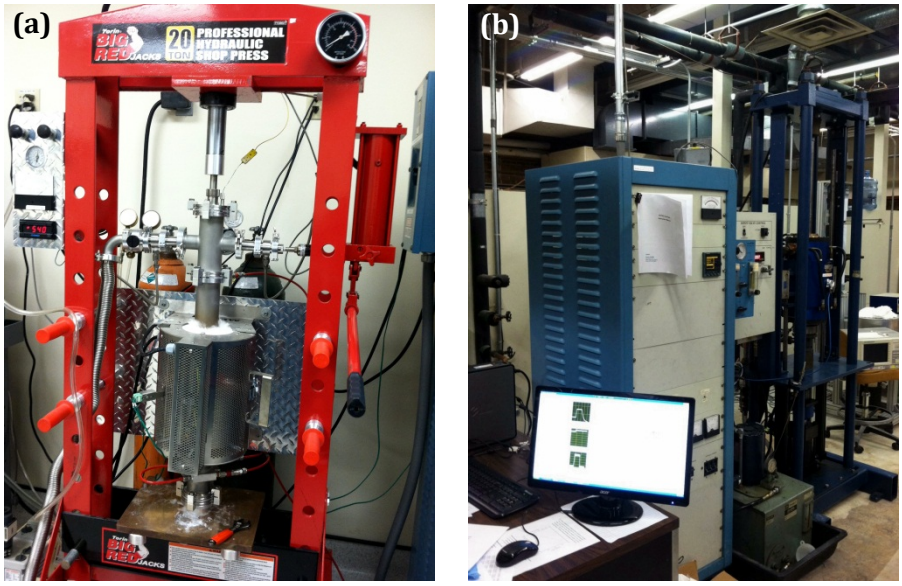

Figure 8: Photographs of the carbon-free hot-pressing system (a) and the commercial Thermal Technology system with data logging (b).

The carbon-free system has the advantage of quicker sample loading and provides a cleaner environment (carbon retains water) for the sample since the powder is contained in a stainless steel die. The commercial system uses a high-purity graphite die and plungers, which can chemically react and reduce the samples. Dies can be transferred from the glove box and held under vacuum in the pressing chamber in under 15 minutes. The Thermal Technology press takes more time to load mainly due to the speed of the furnace elevator and the care taken to position the press rams and die plungers. The advantage of this system is the ability to log data for temperature, applied pressure, and displacement of the pressing rams in a LabView program. Although not as precise as dedicated thermo-mechanical analysis system, the tracking of displacement in the rams at given temperatures and pressures allows us to understand the flow of the powders and sintering behavior of the two compounds.

2.2.3 Hot Isostatic Pressing

Even though hot pressing may result in ceramics with densities near 99% of the theoretical density, it is often necessary to undergo an additional step to collapse the remaining porosity. Calculations using the Rayleigh-Gans-Debye theory, similar to those in the first chapter, show that even very disperse concentrations of pores may severely limit the transparency of a sample. HIPing uses compressed argon to apply isostatic pressures as high as 33kpsi (230MPa) on heated samples. Samples with sufficient density, in which the porosity forms a closed porosity network (i.e. ρ/ρ_{th}> 90%) may reach within fractions of a percent of the theoretical density deeming them virtually pore-free.

Figure 9: Hot Isostatic Press in the Optical Ceramics Laboratory at UCF manufactured by American Isostatic Presses and capable of 1800°C and 230MPa.

2.3 Characterization

2.3.1 Monitoring of Sintering Behavior

When working with compound for the first time, it is important to have some idea of the appropriate sintering conditions (time, temperature, and pressure profiles). To avoid an extraneous number of runs in the hot press before finding appropriate conditions, the hot press in the optical ceramics laboratory at UCF is setup to record densification data. Change in displacement of the pressing rams is monitored to the accuracy of 0.1mm over the entire sintering run using a LabView program. In instances where the powder settles into the die under a moderate

load, the viscoelasticity of the powder can be observed. In the constant pressure and increasing temperature segment of a hot-pressing run, the shape of the strain rate times temperature vs. temperature curve can be related to the activation energy for densification in the material.

In order to extract good data from the displacement curve, it is first important to have a good baseline to account for the thermal expansion and mechanical deformation of the hot press and die components. Only then can the expansion of the powder compact and the strain of the ceramic sample be extracted. This procedure was used for two different hot pressed $BaCl_2$ samples, one using anhydrous powder and one using di-hydrate powder. The first treatment of the raw data is to normalize the baseline run and the sample run in time. The negative of the difference between the sample compaction curve and the baseline compaction curve is taken as the height of the powder compact. The strain rate in the sample is then calculated by Equation 7, where h is the height of the sample and dh/dt is the first derivative of the height in time.

$$\varepsilon' = \frac{1}{h}\frac{dh}{dt} \tag{7}$$

$$\rho = e^{\varepsilon - \varepsilon_{max}} \tag{8}$$

The density (ρ) is then calculated as the exponential of the normalized strain (calculated by differentiating Equation 7) as in Equation 8. This normalization sets the maximum density at the end of the hot pressing run at 100%. This is a reasonable assumption because the measured density of hot pressed samples is typically 95% -99% of the theoretical density in most materials systems. The error in measurement of the density over time is roughly 2% due to the precision of the displacement sensor, the uncertainty in the background subtraction and the deformation of the graphite foil (grafoil) spacers.

Nevertheless, it is also helpful to use the estimated strain in the sample to calculate the activation energy for sintering. The general form of the sintering equation expressed as the strain rate is given in Equation 9[48].

$$\varepsilon' = \frac{HD}{G^m KT}(\Phi P)^n \quad (9)$$

$$D = D_0 e^{-Q_d/RT} \quad (10)$$

$$G = G_0 e^{-Q_g/RT} \quad (11)$$

$$\varepsilon' = \frac{C}{KT} e^{(mQ_g - Q_d)/RT} \quad (12)$$

ε' is the strain rate of the ceramic, H and Φ are constants, D is the diffusivity, P is the applied pressure, G is the grain size (which has its own exponent), and T is temperature in Kelvin. From Equations 10 and 11, it is apparent that both diffusion and grain growth have their own activation energy plus both properties vary with temperature. Because the region of the densification curve examined is at constant pressure, grain size and diffusion are the only variables. Inserting Equations 10 and 11 back into Equation 9 results in Equation 12. Thus with a plot of ln(T*ε') vs. 1/RT, one can estimate the sum of the activation energies as the slope of the curve. If grain growth is assumed to be minimal over the temperature range covered in the plot, the activation energy measured approximates the activation energy for diffusion.

2.3.2 Thermogravimetric Analysis

Earlier in this report, it has been stated that possible sources of reduced optical quality in ceramics include secondary phases and color centers. Many cautions have been taken in the preparation of BaBrI powders to avoid contamination by the ambient atmosphere. However, given its sensitivity to the ambient atmosphere, it is still possible for water impurities to influence the formation of undesirable phases. TGA monitors the weight loss of a sample as a function of temperature. The composition of the off-gas from the TGA is then analyzed with mass-spectrometry. Secondary phases can possibly result from incomplete dehydration. Additionally, the concentration of anion defects may increase due to loss of halogen. TGA was performed on anhydrous powders of both BaBrI and $BaCl_2$ using a TA Instruments Q500 system operated in flowing argon atmosphere. The heating rate was 10°C/min and each compound was taken from room temperature to near its melting point.

2.3.3 X-ray Diffraction

The phase of the starting powders as well as bulk ceramic samples is analyzed using x-ray diffraction (XRD). XRD works on the principle of constructive interference of the x-ray radiation. Waves incident at an appropriate angle to diffract from certain crystallographic planes and be constructively interfered by the waves diffracting from the identical plane below result in spikes of x-ray intensity. On a randomly oriented powdered or non-textured ceramic sample, monitoring the intensity of the diffracted x-ray beam as a function of scattering angle results in a pattern showing peaks at angles where ordered crystallographic planes occur. Each space group has a unique set of peaks. The relative intensities of the reflections are a function of the atom occupying a particular lattice site. With modern searchable crystallographic databases, it is easy to search for published matches to experimental patterns.

The XRD instruments used for this study were a PANalytical system in the Correlated Electron Materials Group at ORNL and a Rigaku D/Max system at UCF, both Bragg-Brentano geometries in which the sample tilts at an angle of θ from the incident x-ray beam, while the detector arm tilts at an angle of 2θ from the sample. The PANalytical system is equipped with an array of CCD detectors to capture the intensity of multiple diffraction angles simultaneously. The PANalytical system also has a rotating sample stage to ensure a representative orientation from all directions in the x-y plane. Both starting powders and bulk ceramics were scanned. Because XRD is a surface analysis technique, samples scanned in the PANalytical system were protected with a Kapton (trade name for a Dupont polymer) sheet, which only contributes a broad background peak at low angles. Protecting samples from the air in the Rigaku system proved more difficult, so the patterns presented in the next section were collected from exposed surfaces.

For the purpose of this study, XRD is used for more than simple phase identification. For instance, in a sample with texture, or preferential grain orientation, the reflections corresponding to preferred directions (aligned perpendicular to the surface of the sample) appear more intense.

XRD may also be used for quantitative analysis of grain size, strain, and crystallographic defects.[49]. In this study, we do not undergo a full refinement of the XRD pattern by a method such as Riedvelt[49]. For the purposes of this study, it is much more efficient to do a simple analysis of the peak broadening by the method pioneered by Scherrer[50].

The Scherrer analysis uses the relationships given in Equations 13 and 14 to approximate the contributions of grain size and strain to the integral breadth (β) of the diffraction peaks.

$$G = \frac{K\lambda}{\beta_{size} cos\theta} \quad (13)$$

$$\beta_{strain} = 4\varepsilon tan\theta \quad (14)$$

The parameter G is grain size, K is the Scherrer constant (taken as 1 in this analysis), and λ is the wavelength of the x-ray beam. By rearranging Equation 13, the total broadening can be expressed as $\beta_{inst} + \beta_{size} + \beta_{strain}$, where β_{inst} is the instrumental broadening. To simplify the plotting and determination of G and ε, the entire expression is multiplied by cosθ to yield Equation 15.

$$\beta cos\theta = \frac{K\lambda}{G} + 4\varepsilon sin\theta \quad (15)$$

Plotting 4sinθ on the x versus βcosθ on the y should give a linear plot for which the slope is ε and G can be calculated from the intercept, provided the contribution of the instrumental broadening is known. An instrumental baseline is commonly found by performing a scan on coarse, strain free powders. The linear plot of Equation 15 is known as a Williamson-Hull plot.

2.3.4 Raman Spectroscopy

Due to the limitations of XRD in identifying trace impurities and subsurface phases, micro-Raman spectroscopy is used as an additional structural analysis tool. Raman is a form of vibrational spectroscopy named after the scientist who first observed the effect of scattered radiation having a wavelength shifted slightly from the incident radiation. The origin of this "Stokes shift" is inelastic scattering, which has come to be known as Raman scattering. Raman scattering is enabled by changes in polarizability that are induced by vibrational configurations. Scattering

occurs at characteristic frequency shifts symmetrically distributed away from the excitation frequency. The red-shifted frequencies (Stokes) are more intense than the blue-shifted (anti-Stokes), and are the ones traditionally detected. Raman scattering is depicted schematically in Figure 10. In a modern Raman system, a sample is excited below its band gap with a laser having a power on the order of a few milliwatts. In the Renishaw micro-Raman system used for this work, microscope objectives are used to focus the excitation on surface features typically between 1μm and 1mm in size. The scattered light is collected and the excitation wavelength is filtered out while the remaining light is analyzed in a spectrometer. The resulting plot shows intensity vs. Raman shift. This differs from another popular vibrational technique, Fourier transform infra-red spectroscopy (FTIR). In IR spectroscopy, one detects changes in the dipolar moment induced by vibrational configurations. The vibrational modes which lead to Raman scattering do not necessarily result in IR absorption. Therefore a distinction must be made between Raman active and IR active vibrational modes.

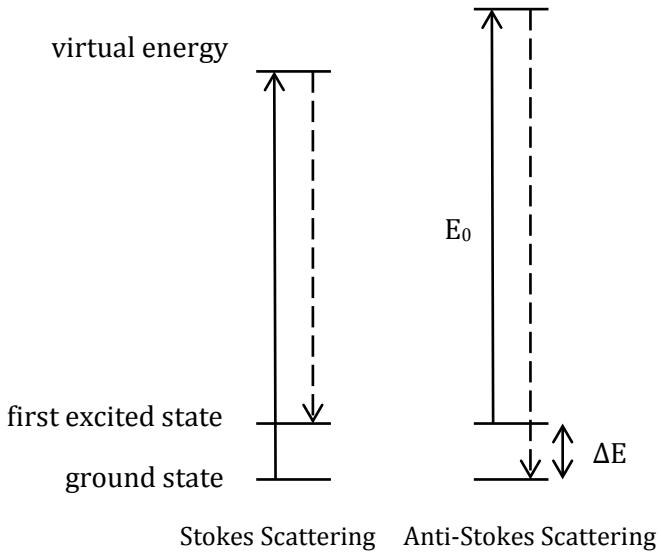

Figure 10: Schematic representation of Stokes and anti-stokes Raman scattering, where ΔE is the energy shift (negative for Stokes and positive for anti-stokes)

Nonetheless, micro-Raman was chosen primarily for the ease of sample preparation. Polishing need not be of high optical quality to obtain good Raman spectra. Additionally, the low transparency of the samples fabricated in the first stage of work on halide scintillators would not have been suitable for He-Ne based FTIR spectrometry, which works best as a transmission (as opposed to reflection) measurement. However, dispersing sample powders in potassium bromide and then pressing results in a transparent sample which can be examined by IR spectroscopy. This method is reserved for future work. The Renishaw micro-Raman spectrometer in the laboratory of Dr. Nina Orlovskya at UCF is equipped with a 514nm laser excitation source and 20x objective with a numerical aperture of 0.2. Thus, the spot size of the laser is roughly 3μm, which is of the same order as the grain size of $BaCl_2$ ceramics estimated by SEM. The laser energy used for excitation is typically 5mJ, which corresponds to roughly 50% of the maximum laser energy. Lower energy is used to make sure the samples were not damaged, because the low transmission of the sample leads to large absorptions at this wavelength. Spectra are collected with an integration time of 30s on a single iteration. Due to the hygroscopic nature of the samples, a thin layer of oil is maintained on the surface to slow down the interaction with the ambient air. A spectrum of the oil is collected as a baseline. The z-position of the laser focus is altered to collect spectra from both the surface and the bulk just below the surface. Focusing deep within the bulk is not possible due to the limited transparency of samples.

2.3.5 Scanning Electron Microscopy

Because the grain size of the samples fabricated by hot pressing is projected to be in the tens of micrometers range, optical microscopy alone is not effective in imaging the surface. To acquire high resolution images of surface features including pores, grain boundaries, and inclusions, it is necessary to use scanning electron microscopy (SEM). Most SEM systems are heavily engineered systems, whose operation is simple in principle, but complex from an engineering perspective. Generating and controlling the electron beam in comparison to the beam

of light used for optical microscopy, is orders of magnitude more difficult. Complex magnetic lenses must be used in place of the glass lenses used to focus visible light. In the most basic terms, an SEM images by refracting electrons off the surface of a sample. Because the wavelength of an electron is much smaller than the wavelength of light, the resolution is greatly improved over light microscopy. The Zeiss Ultra 55 system at UCF is capable of imaging features in the tens of nanometers. Imaging features smaller than this (i.e. atoms and point defects) requires the use of transmission electron microscopy (TEM). TEM was not found necessary at the current stage of this study due to the added complications of sample preparation.

2.3.6 X-Ray Excited Luminescence

Facilities for measuring the x-ray excited luminescence spectra are located at both ORNL and LBNL. The setup consists simply of an x-ray source positioned perpendicular to the edge of the sample and a spectrometer located perpendicular to the sample surface. The use of pulsed x-rays to determine the decay time of the luminescence in Eu^{2+}:BaBrI was carried out at LBNL. Our preliminary tests on $BaCl_2$ ceramic fabrication have not yet included europium dopant for scintillation studies. The typical setup uses a Hamamatsu N5084 Light-Excited X-ray tube. The x-rays are estimated to have a minimum pulse width of 31 ps (fwhm) and an energy in the range of 10-15KeV[51]. The light emission from the sample is converted to an electrical signal with a PMT. Because of the short time scales in the realm of scintillation and luminescent decay, the electrical response of the PMT and subsequent electronics must be quick in order to measure the picosecond time scales needed.

2.3.7 Pulse Height Spectrometry

An important tool for analyzing the brightness and energy resolution of a scintillator is multichannel pulse analysis. In this technique, a monochromatic radioactive gamma ray source is used to build a histogram of pulse height measured in the photo-detector[1]. In order to achieve representative statistics of the scintillation light, a large number of sequential measurements are

often needed (sometimes taking hours to collect). In scintillator research terminology, the x-axis of the spectrum is divided into discrete pulse-height bins, called channels. The plot achieved is a pulse count for each increment of pulse height. The channel number can be related to the energy of the detected light based on the gain of the amplifier in the system.

The interpretation of the pulse height spectrum is demonstrated using Figure 11. The shaded peak is known as the photopeak and the position of its maximum corresponds to the average brightness or pulse height emitted by the scintillator. The width of the photopeak relates to the materials ability to distinguish different energies of radiation, thus a delta function is the ideal case. The numerical value for resolution is calculated as the FWHM divided by the peak position in percent. More to the left, the sharp rise in the spectrum is known as the Compton Edge, named for the contribution of Compton scattering to the registration of counts at energies lower than the energy of the incident radiation.

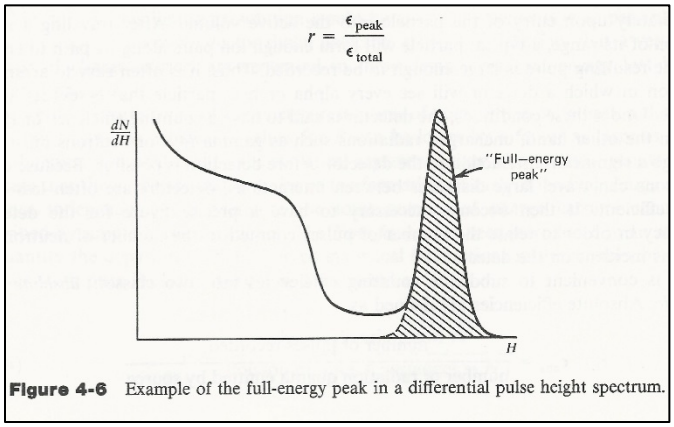

Figure 11: Figure demonstrating a pulse height spectrum taken from Knoll's text[1]. The shaded region is the photopeak from which light yield and resolution are calculated.

The experimental setup for the measurement of pulse height spectra is located at ORNL. Optically polished samples of 5%Eu^{2+}:BaBrI ceramic were mounted with optical coupling grease to the face of the PMT. The radioactive gamma-ray source of either ^{137}Cs of ^{133}Ba is mounted above the sample. Pulse height spectra are collected with a Hamamatsu R6231U photo-multiplier tube and samples are wrapped with Teflon reflector materials to increase the collected light. The signals

from the PMT anode were shaped with a Tennelec TC 244 spectroscopy amplifier and recorded with an Amptek MCA8000-A multi-channel analyzer. The experimental setup is described in more detail elsewhere[26].

2.3.8 Optical Transmission

In order to observe the transmission of the translucent hot pressed ceramics in this study, samples were first ground down to thicknesses between 1mm and 2mm, then polished by hand using silicon carbide papers with ISO grit size designations of P500, P1000, and P2000. When necessary, anhydrous mineral oil was used as a lubricant for polishing. A good quality polish is important to reduce the contribution of scattering from the surface in the measurement of optical transmission. In the case of both $BaCl_2$ and BaBrI, many samples were translucent to the level that printed text could be read through a backlit sample placed flat against the paper. A standard halogen flashlight was used for backlighting. For a more quantitative analysis of transmission, the Varian Cary 500 spectrophotometer in UCF/CREOL was used.

The Cary spectrophotometer uses a broad spectrum xenon lamp and an optical grating to scan through a wavelength range of 190nm – 3300nm. The instrument has a dual sample chamber, so a background spectrum is collected at the same time as the sample spectrum acquisition. The length of a scan is roughly 15 minutes, so hygroscopic samples were not protected from the air during a spectral acquisition. However, they were kept in mineral oil or in the glove box until the moment they were transferred to the spectrophotometer's sample holder.

3. RESULTS AND DISCUSSION

3.1 Sample Preparation

A total of 10 BaBrI samples and 5 $BaCl_2$ samples have been fabricated. In the early stages of studying these ceramics it is important to cover a broad range of processing conditions to optimize the densification of these materials. Appendix 1 lists all the samples fabricated for this study along with a description of their processing conditions and characterization. The most obvious effect on the processing of BaBrI thus far is the exposure of the precursor powders to air. When the process is made cleaner by working in a cleaner glove box and pre-heating the dies, the translucency of samples pressed from the purified BaBrI powder is improved. In the case of $BaCl_2$, the biggest effect on the first impression of sample quality is the commercial supply of powder. Lower purity (99%) di-hydrate powders produced opaque white samples, while higher purity powders of both the di-hydrate and anhydrous nature, sintered under similar conditions, resulted in translucent samples. At this time the differences in manufacture and thus the sources of impurities in the three batches of $BaCl_2$ powder are unknown.

3.2 Monitoring of Sintering Behavior

The plot of temperature, density, and applied load versus time for a $BaCl_2$ ceramic is presented in Figure 12. This densification plot corresponds to a sample fabricated from anhydrous powder and sintered at a temperature of 850°C for six hours. A dehydration step is added at 250°C to ensure complete removal of water. The pressure applied to the sample is increased from1MPa to 47MPa once the dwell temperature has been reached. The densification of the sample is complete soon after the temperature reaches its dwell of 850°C and before the pressure has reached its maximum 47MPa. Similar behavior is seen in a sample fabricated from anhydrous starting powder and sintered for six hours at 750°C (plot not shown).

Table 5: Activation energies of $BaCl_2$ calculated from the densification data compared to the activation energy calculated from high temperature conductivity data.

Sample	Calculated Q (kJ/mol)
$BaCl_2$ ceramic from di-hydrate	23
$BaCl_2$ ceramic from anhydrous	27
$BaCl_2$ resistivity data	57

The calculated strain rate (ε') in the sample is used in both cases to estimate the activation energy for mass transport (densification) according to the equations presented in the previous section. The 1/RT versus ln(T*ε') plot for the sample hot pressed at 850°C is shown in Figure 13.

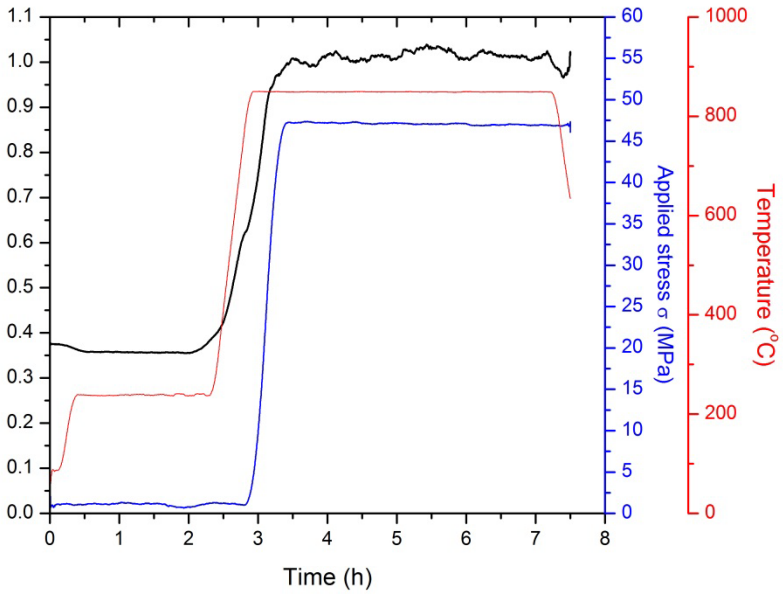

Figure 12: A treated hot press dataset showing the density (derived from the displacement), temperature, and applied load over time.

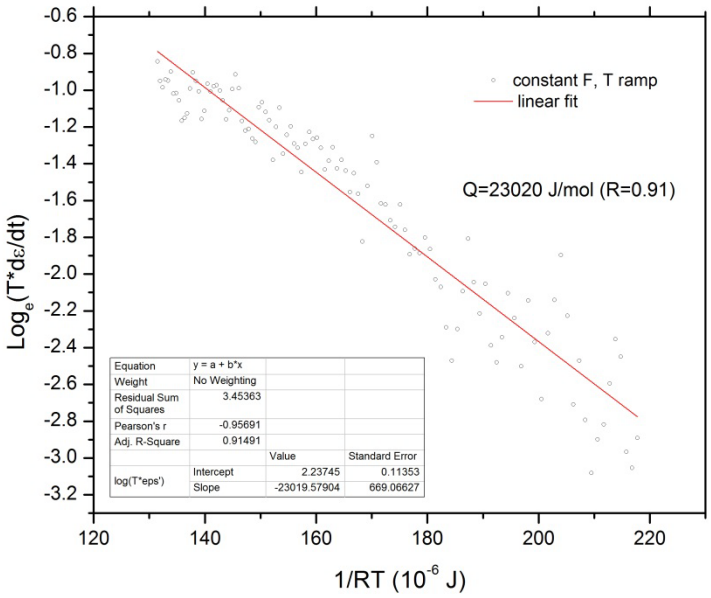

Figure 13: Graphical determination of the activation energy for densification in $BaCl_2$ hot pressed at 850°C.

The estimated activation energy for the di-hydrate powder pressed at 850°C is 23KJ/mol while the same calculation for the anhydrous powder pressed at 750°C is 27KJ/mol as reported in Table 5. Activation energy should not vary with the sintering temperature or between different batches of powder, assuming the energy corresponds to pure $BaCl_2$ and is not altered by impurities. The results so far suggest that the sintering of the anhydrous and dehydrate powders follow a similar mechanism after complete removal of water. However, these energy values are taken with caution, as they can be highly dependent on the manipulation of the raw data file (i.e. background subtraction, smoothing, and differentiating). No study of the densification of $BaCl_2$ has been found in the literature.

Nevertheless, electrical resistivity data can be used to estimate the activation energy for ionic diffusion assuming the ionic transport mechanisms are similar in both cases. Luckily the resistivity of $BaCl_2$ has captured interest recently due to the large observed decrease in resistivity as the orthorhombic form transforms to the cubic at high temperatures. Figure 14 below shows four data points taken from an article by Hull et. al. and fitted with the typical Arrhenius relationship[52].

The activation energy calculated from the electrical resistivity values is of the same order of magnitude as the values calculated from hot pressing data. The lower values of the activation energy for the hot press could be explained by the presence of impurities that aid in the transport of barium and chlorine ions during sintering. This comparison is also treated with caution because the electrical conductivity of $BaCl_2$ at high temperatures has been reported to arise predominantly from the migration of Cl^- ions and not Ba^{2+} ions. Conversely, the ionic transport during densification is ambipolar. In future experiments where purifying agents may be added to the powders it will be interesting to continue monitoring the sintering behavior. Also, as the full range of sintering conditions is explored, especially lower temperatures, the effects of pressure may be more easily modeled in the constant temperature/increasing pressure regime.

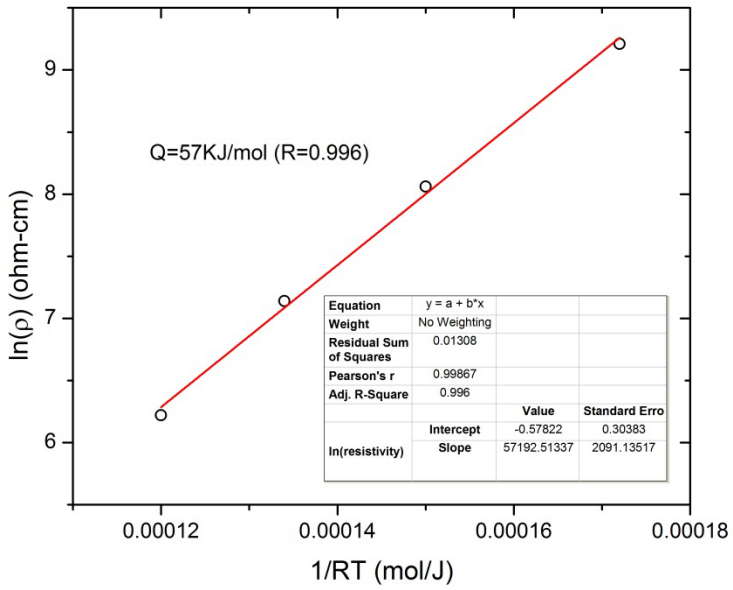

Figure 14: A plot of 1/RT versus the logarithm of electrical resistivity for data points extracted from Hull's article.

Additionally, measurement of the grain size of fully dense ceramics following hot press runs will allow the separation of Q_g from Q_d.

3.3 Hygroscopicity of Powders

The total percentage weight gain over time in air is plotted for both BaBrI and $BaCl_2$. The behavior of SrI_2 is also plotted for the sake of comparison.

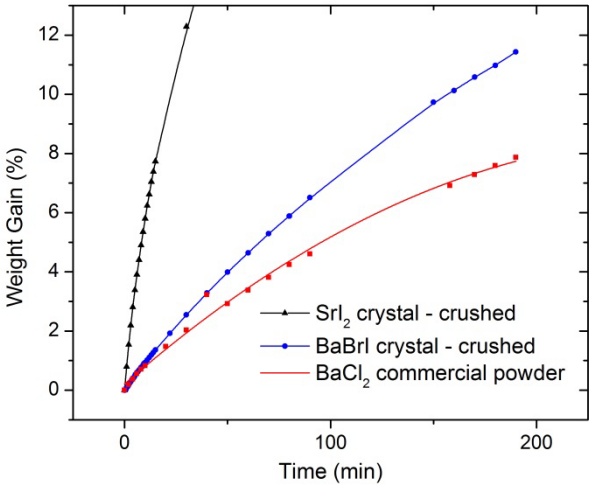

Figure 15: Weight gain of halide powders. All powders were crushed to similar particle sizes. Colorless crystals were grown in-house.

SrI_2 clearly shows the highest hygroscopicity, which is in agreement with the literature[27]. $BaCl_2$ shows slightly lower weight gain than BaBrI. Based on a similar study shared privately by LBNL, many of the halide compounds reach a saturation point above 20% weight gain. However, for the purpose of this work, reaction in the time span of roughly 0-30 minutes, while the powder is loaded for pressing, is the main concern. Powders studied had particle sizes of roughly 20μm. If finer milled powders are used for the purpose of achieving smaller grain sizes in the final ceramics, weight gain is expected to happen more quickly due to the higher surface area in contact with the ambient air. Studies on fine powders may be necessary in the future if finer grained ceramics are necessary to gain transparency. As mentioned earlier, the hydration of $BaCl_2$ is reported to be reversible. This has been observed qualitatively as saturated $BaCl_2$ powders lose weight once they are transferred back to the glove box. Further discussion of the dehydration of the barium halide compounds is found in the thermogravimetric analysis section.

3.4 Thermogravimetric Analysis

The TGA curve for BaBrI is presented in Figure 16. This 93mg sample of BaBrI purified powder was measured at a heating rate of 10°C/min from room temperature to 600°C. Five distinct regions of weight loss beginning at room temperature, 50°C, 100°C, 200°C, and 450°C are observed. Mass spectrometry of the off-gas is not available, so identity of the species lost in each step is not clear. One species sure to be present is water. It is known that strength of the hydrate bonds in BaBrI is be much higher (based on the documented behavior of SrI_2) than those in $BaCl_2$[27]. SrI_2 goes through three stages of dehydration (SrI_2-$6H_2O$, SrI_2-$2H_2O$, and SrI_2-H_2O), losing its final water just before 400°C. Based on this data, BaBrI may follow a similar stepwise dehydration mechanism. With the sample being a purified BaBrI powder which was stored in a glove box, only a small amount of water is believed to be present. According to the TGA curve, the lost water content is just above 1.8% by weight, assuming all water is lost by 400°C.

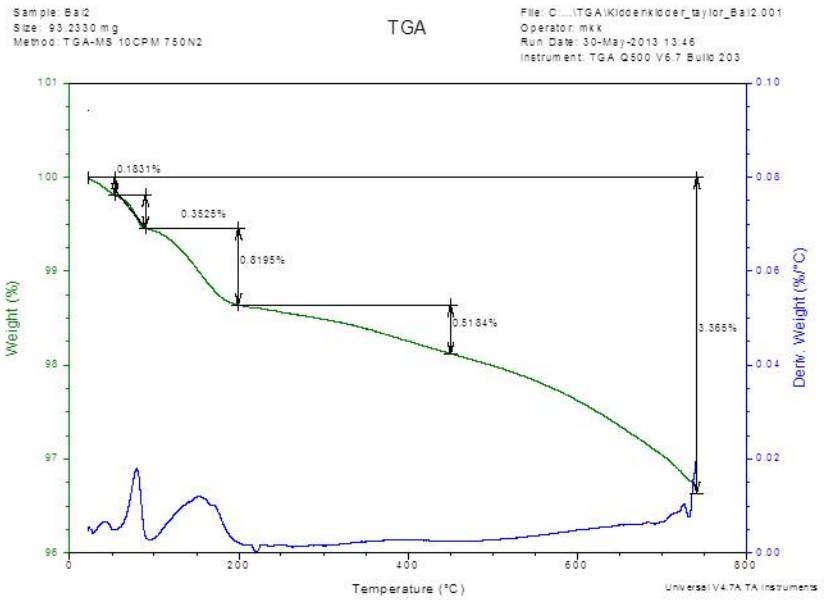

Figure 16: TGA curve for BaBrI showing percent weight loss versus temperature. The derivative of the curve easily identifies changes in slope.

Based on the results found by Raman spectroscopy, one can project that some samples have retained water (hydrate and –OH groups) in the bulk. Contrary to the observed dehydration behavior of the iodides, $BaCl_2$ has been documented as a reversible process[47,53]. TGA data on the hydrate will be needed to confirm this, because the method used in the literature for measuring complete change of the phase to $BaCl_2$ from di-hydrate starting powder is XRD on a heated stage. This technique may not be sensitive enough to detect the traces of water which are of concern to transparent ceramics. Again, the results of Raman spectroscopy already suggest that the process is not completely reversible.

Looking at the continued weight loss of BaBrI as temperatures move towards the melting point (850°C), it is not expected that water will continue to be lost. The loss of iodine at these higher temperatures has been documented for SrI_2 in the same study mentioned above. If one suspects iodine vapor loss in the case of BaBrI, deviation from stoichiometry and the formation of anion defects become a possibility. These defects can be associated with color centers, the simplest of which is depicted in the schematic of Figure 17.

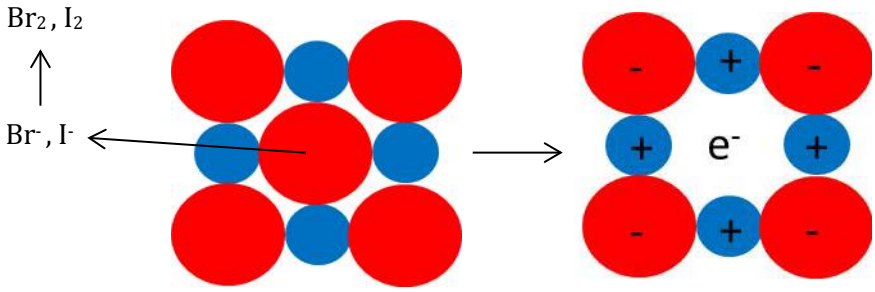

Figure 17: Schematic of F-center creation due to anion vacancies created by the loss of halogen gas

3.5 X-ray Diffraction

The first pattern shown in Figure 18 was collected from a barium bromide iodide sample using the PANalytical system. The 2θ range is 15° to 70° and a step size is 0.017°. The positions of

the peaks for the Eu^{2+}:BaBrI ceramic sample are a good match to the reference and to a pattern calculated using FullProf software. There is a slight shift of the ceramic pattern toward lower angles. Considering the orthorhombic lattice belonging to space group 62, the Eu^{2+} ion is expected to substitute directly for the Ba^{2+} ion [42]. An 8-coordinated Ba^{2+} ion has an ionic radius of 1.42Å compared to 1.25Å for and 8-coordinated Eu^{2+} ion[41]. The presence of smaller ions in the lattice leads to a reduction of the lattice parameters. The distortion of the lattice from its ideal shape is not uniform, so the spacings between the refracting planes (d spacing) are not necessarily affected uniformly. The change in the lattice parameters is estimated using Equations 16 and 17. The first equation is just a weighted average of the of the lattice parameter calculated in the reference refinement and the unit cell containing one Eu^{2+} ion in place of a Ba^{2+} ion.

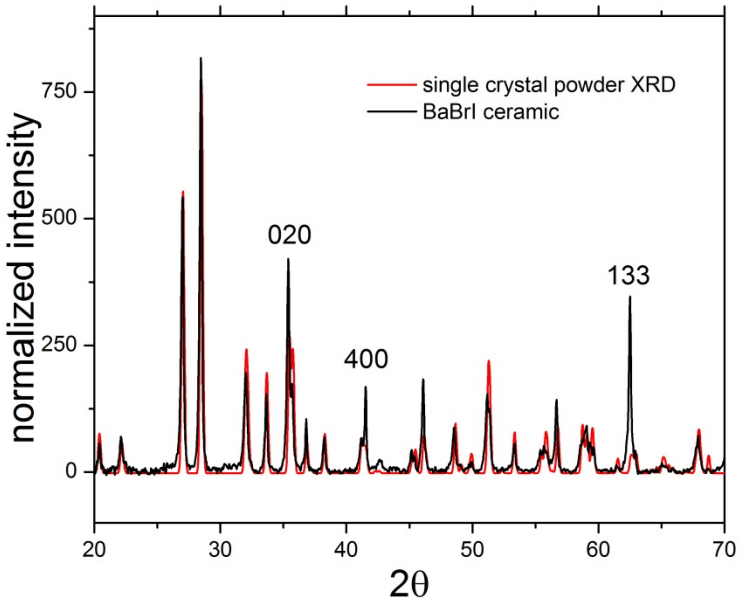

Figure 18: XRD pattern of a Eu^{2+}:BaBrI ceramic compared to the reference of a crushed single crystal powder XRD pattern from the literature.

Equation estimates the change in the lattice parameter as the difference in atomic radius of Eu^{2+} versus Ba^{2+}.

$$at\%_{dopant} \times l_{dopant} + at\%_{ref} \times l_{ref} \quad (16)$$

$$l_{dopant} = l_{ref} - \Delta r \quad (17)$$

The pattern calculations based on an equal change in each of the lattice parameters due to doping is shown in Figure 19. The other major input parameters for this calculation are the atom types, approximate positions, and occupancies based on space group 62. The FullProf program calculates selection rules and scattering efficiencies given the input to produce a pattern.

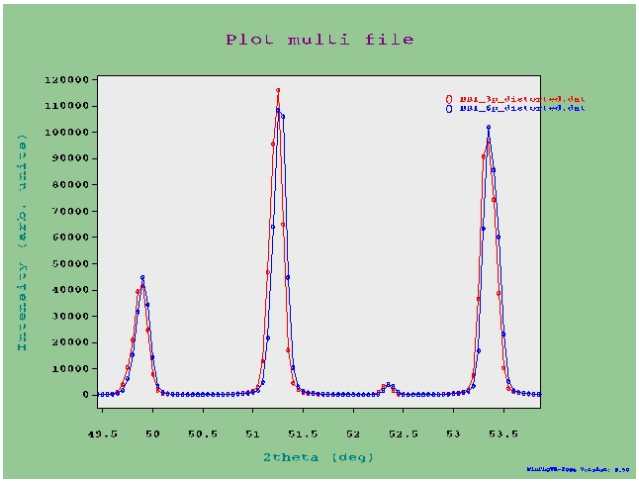

Figure 19: Calculated XRD pattern of BaBrI from 2θ=49.5 to 54.0 showing the shift due to an increase in doping from 3 wt% (red) to 6 wt% (blue).

The magnitude of the calculated shift varies from +0.01°±0.005° at low angles to +0.03°±0.005° at higher angles. The reason for the increase in shift as a function of angle (2θ) is the non-linearity of the sine function in Bragg's Law. The shift is actually based Bragg's Law (nλ=2dsinθ), where the d spacings are inversely proportional to the sine of the angle of refraction (and the angle itself). Thus, a shift towards higher 2θ angles is expected for the 6% Eu^{2+} doping concentration in the ceramic relative to the reference, which has only 3% doping. The shift observed in Figure 18 is in the opposite direction than would be expected for the difference in doping and also greater in magnitude (>0.1°). For now, one may assume that the instrumental shift has not been adequately accounted for in our experimental 6%Eu^{2+}:BaBrI pattern.

An additional feature of the patterns in Figure 18 is the difference in the relative intensities of the ceramic peaks compared to those of the reference pattern. For instance, the peaks at 2θ~35, 41.5, and 62.5 are much more intense in the ceramic pattern versus the single crystal pattern. Several other peaks, including that at 2θ~51, appear less intense in the ceramic versus the reference. Because the reference pattern was collected from a crushed crystal, it is assumed that diffractions from each crystallographic plane are present in equal proportions. This rise and fall of certain peaks in the ceramic pattern relative to the identically positioned peaks in the reference pattern suggests preferential orientation of grains. The Miller indices of the peaks appearing more intense in the ceramic sample are shown in Figure 18. These indices correspond to the (020), (400), and (133) planes respectively. Furthermore, the (020) plane corresponds to the cleavage plane of the cotunnite mineral($PbCl_2$) , which adopts the same crystal structure as BaBrI[54]. Cleavage along these closest packed planes is easily visualized in a unit cell oriented parallel to these closest packed planes as in Figure 20. The cleavage of particles in the hot press is possible due to the high pressures realized at particle interfaces. The preferred settling of cleaved particles may explain the other preferred directions, (400) and (133), which are parallel or nearly parallel to the cleavage planes. This could indicate that sheared particles have preferential directions for settling. The evolution of texture for hot pressed barium halides is also supported by the parallel fracture surfaces observed in an SEM image of $BaCl_2$.

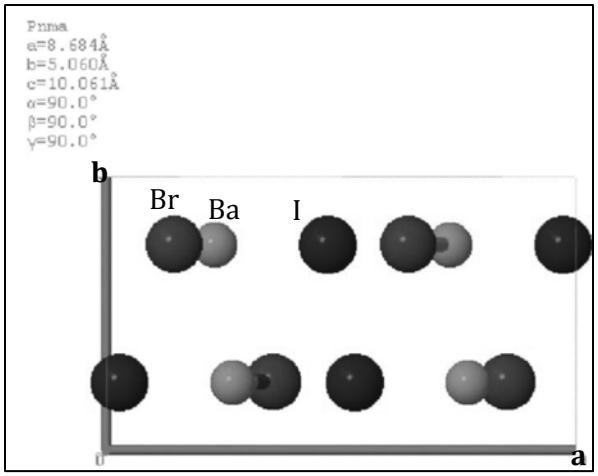

Figure 20: Looking down on the c-axis at the stacked (020) planes of a BaBrI crystal. The (100) direction is a favorable shear direction.

Finally, the broadening of the peaks from the pattern shown in Figure 18 was analyzed by the Scherrer method, originally devised in the early 1900s[50]. The resulting analysis, described in the Experimental Methods, showed no significant contribution of grain size or strain to peak broadening. The grain size is not a factor because its magnitude (4μm) contributes less to the broadening than the typical instrumental broadening. The points for 17 peaks taken for the Williamson-Hull plot did not show good linear correlation, thus the one pattern of BaBrI analyzed does not show evidence of strain broadening. Because residual strain in hot pressed ceramics has been observed in the past, it will be interesting to analyze future patterns for broadening[55]. Strain can affect the environment around the dopant, leading to changes in the scintillation and annealing steps may be needed to relieve it.

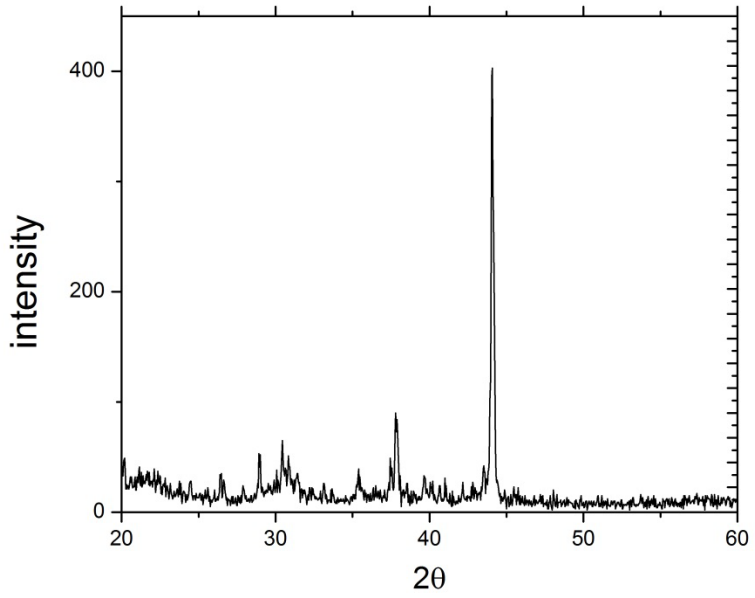

Figure 21: X-ray diffraction pattern collected on the Rigaku system for an unprotected sample of $BaCl_2$. The reference peak position and intensities (taken from MDI JADE database) closely match monoclinic $BaCl_2$-$2H_2O$ (space group 14).

The study of $BaCl_2$ ceramics by x-ray diffraction in the Rigaku system has not yet been optimized. Kapton sheets were not available for use in protecting the sample from the air, so cellophane was used in its place. Even so, securing the protective layer in the available sample holders was difficult. Patterns collected from samples protected in this manner showed a high contribution of the background and the peaks arising from the ceramic were difficult to resolve. Patterns were also collected from unprotected samples, which had been exposed to the air for longer than one hour prior to loading and during scanning in the XRD. These patterns showed low signal to noise ratio and low raw intensity counts. These are typically instrumental artifacts possibly arising from insufficient calibration and/or inappropriate positioning of the sample. Nevertheless, the patterns show a predominant hydrate phase belonging to a monoclinic crystal system as seen in Figure 21. Because the chemical quality of the sample surface is important in XRD, these patterns were not representative of the bulk. Other methods of protecting the sample

from the air during acquisitions are currently being investigated. Design of a new sample holder based on that from the PANalytical system is also in progress.

3.6 Raman Spectroscopy

The $BaCl_2$ samples fabricated from anhydrous powders versus di-hydrate powders showed significant differences in their Raman spectra. Figure 22 shows the spectra collected from a ceramic made from anhydrous starting powder. The three spectra presented correspond to the oil background, the surface, and the bulk just below the surface as described in the experimental procedure section. Subtraction of the contribution from the oil in the spectra of the ceramics was difficult, because the intensities of the oil peaks relative to the peaks originating from the ceramic were different in the surface ceramic spectrum versus the bulk ceramic spectrum. The bands occurring at frequencies below $250cm^{-1}$ are attributed to the Ba-Cl bonds in the orthorhombic crystal. From the fitting of a calculated spectrum to experimental data in a recent article by Bohley, the bands are assigned according to the Table 6[56]. Figure 22 (b) shows the frequency range where these modes fall. The nomenclature of the modes in the table is based on Herzberg's formulas for the electronic states of a given molecule, which is treated in great detail in his seminal work, *Electronic Spectra and Electronic Vibrations of Polyatomic Molecules*[57]. The vibrations from the $BaCl_2$ are expected to be more intense in the bulk spectrum versus the surface spectrum, however the combination of the high oil background and the low transparency seem to lead to only slight a difference in the absolute intensity of these bands. The peaks present in Figure 22(b) match up well with those reported in Table 6, with the exception of the low intensity peak at $230cm^{-1}$.

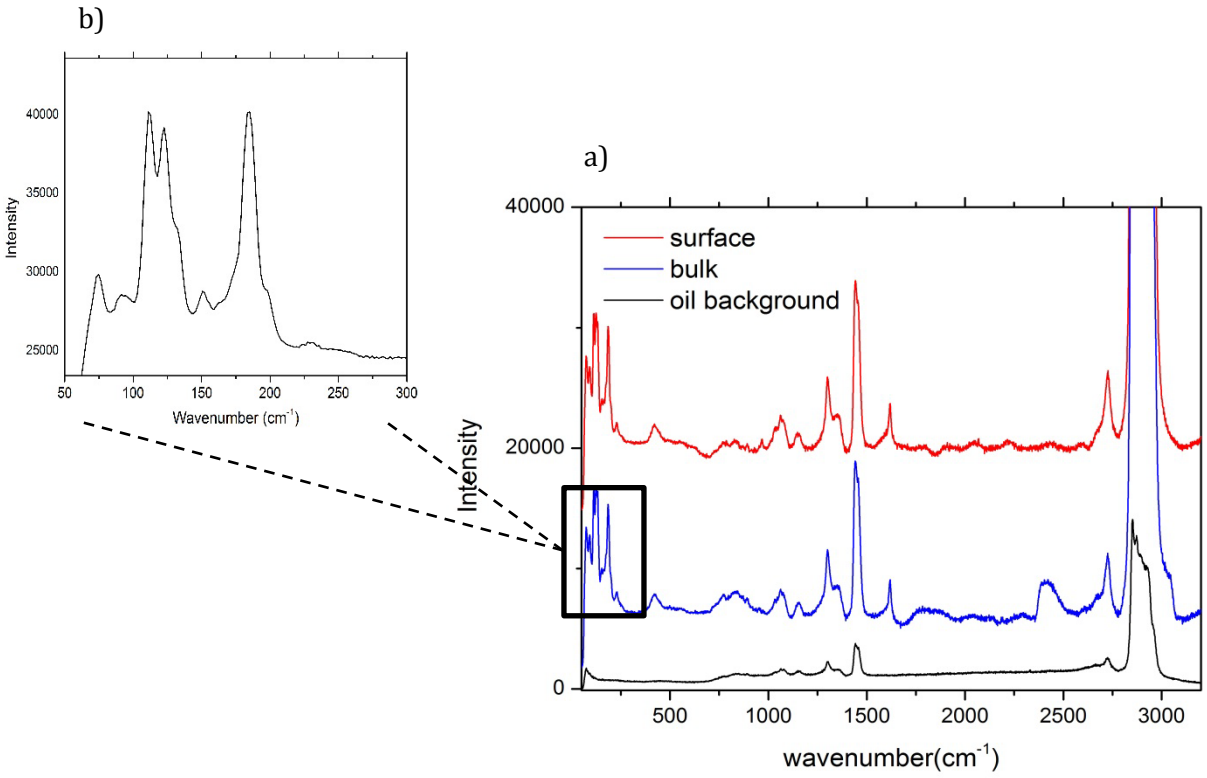

Figure 22: (a)Raman spectra collected from a $BaCl_2$ sample fabricated from anhydrous $BaCl_2$ powder and (b) a replot of the bulk spectrum the in frequency range of the Ba-Cl modes.

This peak falls close to a reported peak from $BaBr_2$-H_2O (monohydrate)[58]. Additionally, peaks centered at 432cm^{-1} and 838cm^{-1} are observed in both Figures 22 and 23 (anhydrous and dehydrate respectively). These are possibly attributable to Ba-O modes based on the similar positions observed in a study of barium oxide mixtures[59]. At this time, none of the other features have been assigned. For future Raman studies, it will be helpful to scan to slightly higher wavenumbers in order to capture the vibrations of –OH. Cation to hydroxide bond vibrations have been calculated to appear above 3300cm^{-1} by Hermansson, Lutz, and others. Finally, molecular water vibrations are expected to occur near 3000cm^{-1}, which is likely a major contribution to the oil spectrum. In the future, high purity and anhydrous oil may be used to prevent the overlap of the background on possible features in the ceramic.

Table 6: Tabulation of Raman vibrational frequencies in $BaCl_2$ from the Bohley publication.

TABLE II. Calculated wave numbers (values in cm^{-1}) of the Raman-active zone-center phonon modes in orthorhombic *Pnma* $BaCl_2$, $BaBr_2$, and BaI_2 and the assignments to their symmetry-adapted types. For comparison the $BaCl_2$ modes measured by Sadoc *et al.*[7] and Pfau *et al.*,[6] and the $BaBr_2$ modes measured by Monberg *et al.*[8] and Pfau *et al.*[6] are given in parentheses (see the text). No Raman measurements were available for BaI_2.

A_g	B_{1g}	B_{2g}	B_{3g}
$BaCl_2$ *Pnma*			
54 (57,55)	60 (61,60)	95 (98, —)	54 (57,55)
77 (77,76)	117 (112, —)	117 (113,113)	127 (123, —)
110 (111, —)	187 (186, —)	127 (121, —)	187 (186,186)
131 (124,125)		149 (151,152)	
176 (175,175)		170 (—, —)	
197 (191,200)		202 (198, —)	
$BaBr_2$ *Pnma*			
44 (47,47)	49 (50, —)	69 (74, —)	45 (—, —)
62 (62,62)	76 (84, —)	86 (85, —)	84 (88, —)
78 (75,75)	126 (126, —)	99 (—, —)	125 (114,125)
92 (85,85)		108 (—, —)	
118 (115,113)		116 (125, —)	
137 (134,133)		133 (135, —)	
BaI_2 *Pnma*			
38 (—)	46 (—)	55 (—)	41 (—)
50 (—)	59 (—)	69 (—)	70 (—)
61 (—)	104 (—)	74 (—)	102 (—)
71 (—)		86 (—)	
94 (—)		99 (—)	
119 (—)		116 (—)	

The second set of spectra, presented in Figure 23, were collected from a sample fabricated from the di-hydrate powder. Over the collection of many spectra from 2 different samples which started from di-hydrate powder, the conclusion is that the spectra do not consistently show different and identifiable features to the anhydrous samples. The final spectra presented in Figure 24 shows the low frequency region of the expected vibrations of BaBrI. The BaBrI bands are in the same frequency range to those of $BaCl_2$, however their exact positions and relative frequencies differ slightly due to the differences in bond length, bond angle, and atomic mass. Extensive analysis of the BaBrI Raman spectra has not been performed at the time of publishing this report.

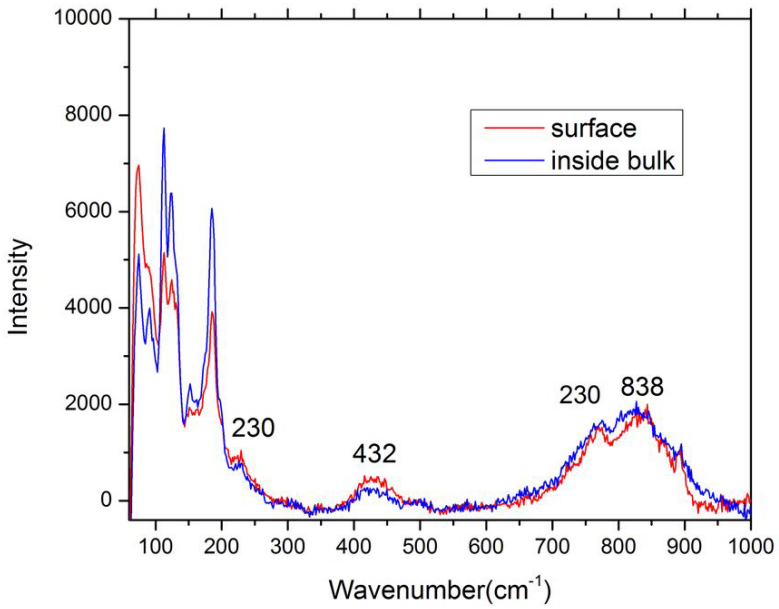

Figure 23: Raman Spectra from the bulk and surface of a hot pressed $BaCl_2$ sample fabricated from anhydrous starting powder.

As more experience is gained with both the Renishaw system and the sensitive samples, more definitive analysis should be possible. At this point, the excitation spot size used is on the same order of magnitude as the grain size. Because the surface is not polished, grain boundaries are not visible and probing individual grains is not possible. Thus in this stage of the study it makes more sense to use a lower magnification to acquire spectra which are a better average representation of the ceramic. Another area of future interest is the identification of crystal defects by Raman spectroscopy[60]. If the concentration of defects is high enough, a signature for the defective bonds should appear at a different frequency than the fundamental modes associate with a 'correct' bond. Based on the appearance of the $BaCl_2$ and BaBrI samples and the analysis by TGA, it has been postulated that crystal defects, i.e. color centers are present. The use of Raman spectroscopy as a tool to identify color centers would be an added benefit of the technique.

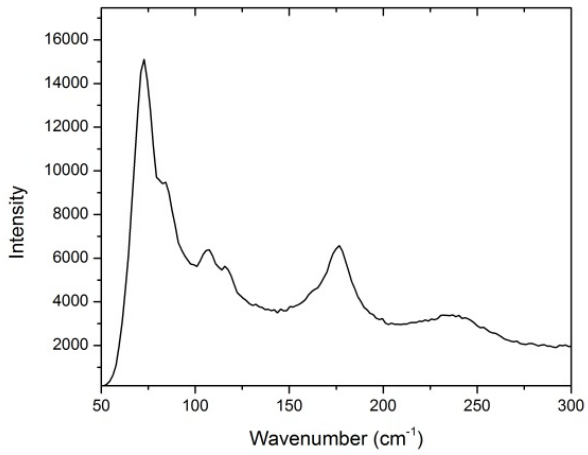

Figure 24: Raman spectra of a 6%Eu^{2+}:BaBrI sample shown in the low frequency range of Ba-Br and Ba-I vibrations.

3.7 Scanning Electron Microscopy

Images of the $BaCl_2$ di-hydrate starting powder and two different ceramic samples were captured in the SEM. The ceramic in Figure 25 fabricated from the di-hydrate powder. The hot pressing schedule included a dehydration step 250°C for six hours and then sintering at 800°C for 6 hours with an applied pressure of 45MPa. Figure 25 also shows the starting powder, which has large agglomerates over 100μm in diameter. The fractured edge of the ceramic in the other image displays a surprisingly small grain size. The intercept method was used to come up with an estimated grain size of 3μm 1μm. Thus, the large particles seen in Figure 25 (top) are indeed large agglomerates composed of much smaller particles. The polishing and ethanol etching of the surface of a ceramic sample to image the grain boundaries did not yield good images. The ethanol used to etch the polished surface reacted too vigorously resulting in a wavy surface with no clear definition of the grain boundaries. Using other etchants or even taking advantage of the moisture in the air to etch the surface will be investigated in the future.

The grain size for the second ceramic $BaCl_2$ sample fabricated from the anhydrous powder was also determined with SEM. The 4μm size is comparable to the size of the grains in the di-

hydrate ceramic shown in Figure 25. This is the case even though the starting powder for the second sample has a much smaller particle size.

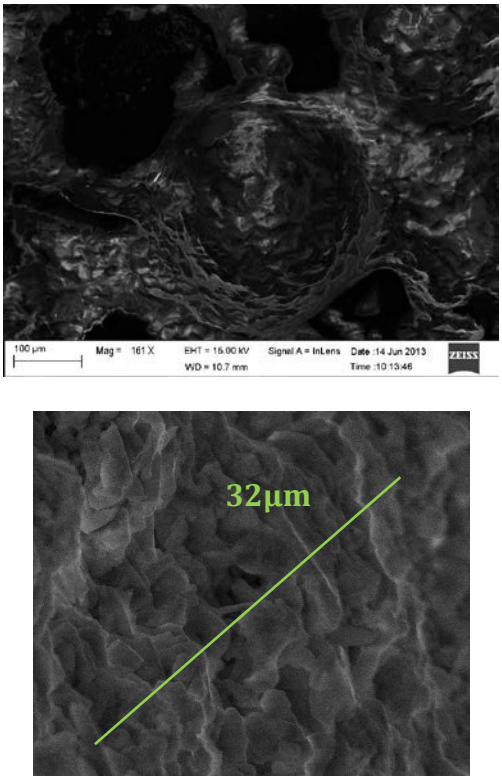

Figure 25: SEM images of coarse $BaCl_2 - 2H_2O$ starting powder (top) and a ceramic made from the powder (bottom). The line used to count grains by the intercept method is shown.

The final picture presented shows the shearing of the grains along parallel directions in a $BaCl_2$ ceramic. This supports the evidence of the possibility of texturing in hot pressed ceramics which was observed in the XRD for BaBrI.

In the initial investigations of $BaCl_2$ with SEM, the energy dispersive spectroscopy (EDS) feature on the Zeiss system was not utilized. This is an elemental analysis tool typically accurate to roughly one weight percent. In the future, it will be interesting to probe the surface for impurities by using this technique. EDS analyzes the energy of scattered electrons, which can be correlated to the atomic weight of the atom from which it has been scattered. This elemental analysis will be a good compliment to the ongoing studies using Raman spectroscopy.

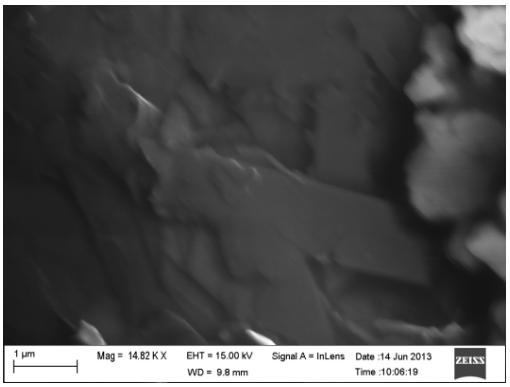

Figure 26: Shearing of grains along parallel directions observed in an SEM image of $BaCl_2$.

3.8 X-Ray Excited Luminescence

The x-ray excited emission spectrum of BBI ceramic and single crystal samples is presented in Figure 27. The emission of the ceramic is centered at 418nm while the crystal is shifted slightly towards lower wavelengths by approximately 4nm. The ceramic emission line is also significantly broader than that of the single crystal.

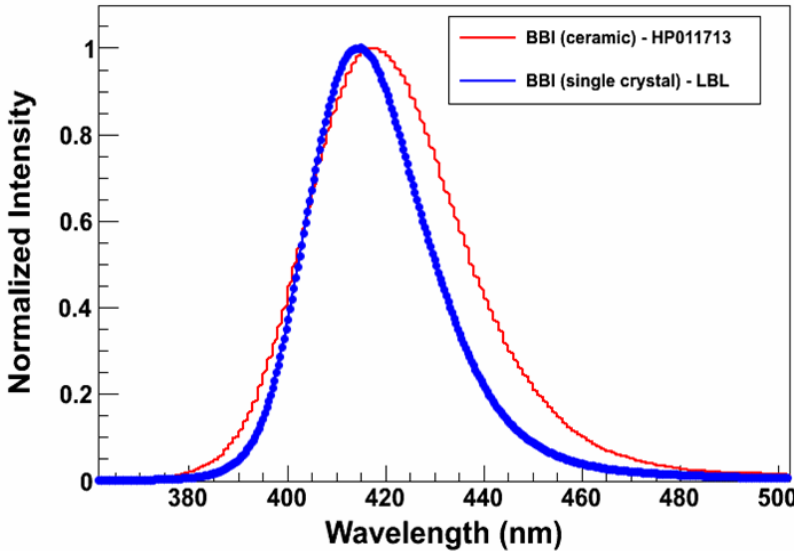

Figure 27: Comparison of x-ray excited emission in BBI ceramic versus single crystal. The ceramic was measured at ORNL and the single crystal at LBNL.

The presence of one single broad emission line between 380nm and 460nm in both the x-ray excited and optically excited (not presented here) spectra is an improvement over the first

measurements reported from 2002[61,62]. These early measurements showed a much broader emission consisting of at least 3 component bands. The authors attributed the multiple bands to the occupation of the Eu^{2+} ion at multiple Ba^{2+} sites in the orthorhombic lattice. However, the current understanding of the lattice identifies only one barium site with coordinates of x=0.7696, y=0.2500, and z=-0.1247 with respect to the three lattice parameters. The atom has a multiplicity of 4 in the lattice[42]. The nature of the shift in position of the emission band is not yet known.

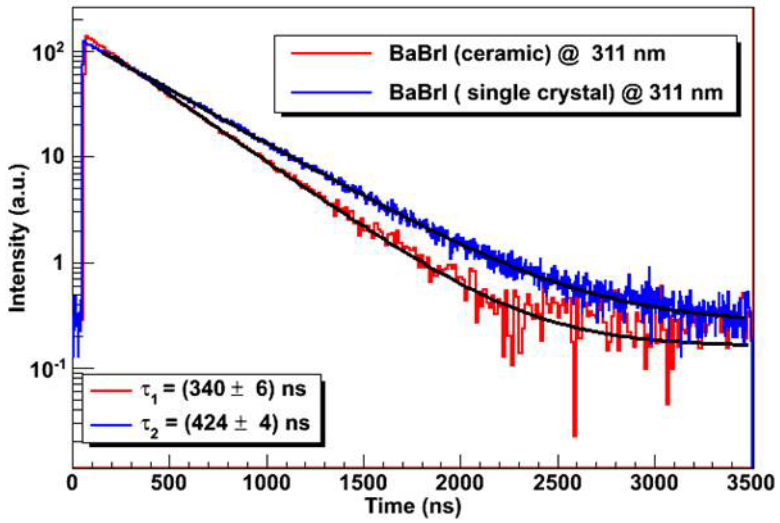

Figure 28: Decay time of ceramic and single crystal BaBrI measured in the pulsed x-ray system at LBNL. τ is calculated from the fit to an exponential function.

The time response of a 6%Eu^{2+}:BaBrI ceramic and a 6%Eu^{2+}:BaBrI single crystal were measured using the pulsed x-ray system at LBNL. The fitted exponential curves show a slightly faster decay in the ceramic versus the single crystal. At this point there is no clear evidence for any particular difference in the decay mechanisms that would explain this difference in decay time.

3.9 Pulse Height Spectra

The initial pulse height spectra collected from 6% Eu^{2+}:BaBrI do not show a photo-peak. This can be correlated mainly with the low transmission of the samples seen in the next section. The scintillation light is not able to escape the sample without encountering excessive scattering events. At this point in the study, the absence of a photo-peak is not a grave concern because the

main tasks are to improve transparency and eliminate color centers. The addition of a dopant to activate $BaCl_2$ and the continued work on Eu^{2+} doped BaBrI will necessitate the continued study of pulse height spectra to calculate light yield and energy resolution.

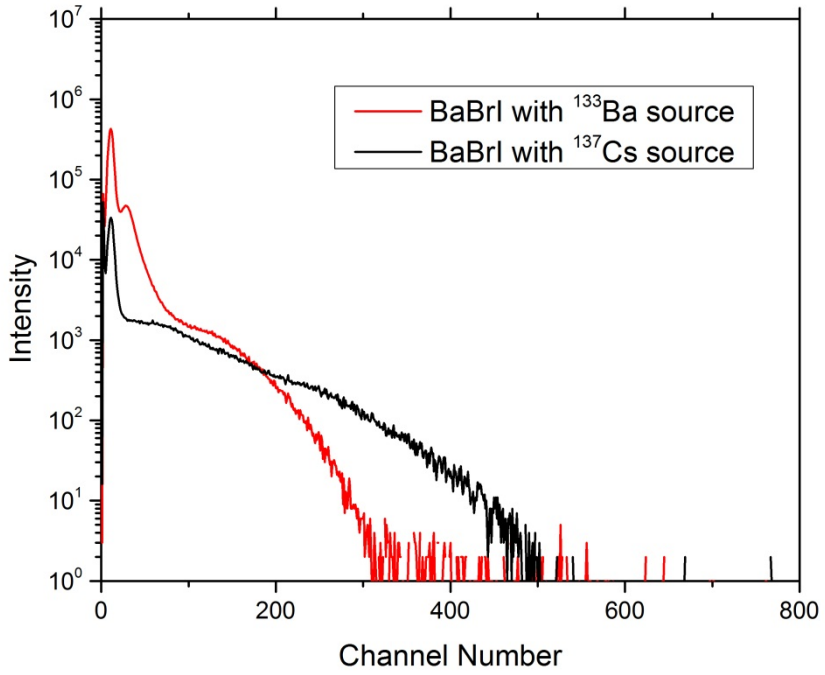

Figure 29: Pulse height spectra of BaBrI using both ^{133}Ba and ^{137}Cs gamma ray sources.

3.10 Optical Transmission

The visual appearance of hot pressed samples after rough polishing has varied vastly in the course of the six months of this project. The most transparent BaBrI samples achieved still have a strong brown color as shown in Figure 30(a). Also, the birefringence of the rather large grains (100μm as a rough estimate) is seen by the inhomogeneous color of the sample. $BaCl_2$ samples have typically exhibited a grey color. Also of note are the darker spots on the sample in Figure 30 (b), which appear to be present in the bulk as well as the surface. Attempts to determine structural differences between these regions and the bulk ceramic by micro-Raman spectroscopy have been unsuccessful. EDS may also be helpful in determining the nature of these inhomogeneities.

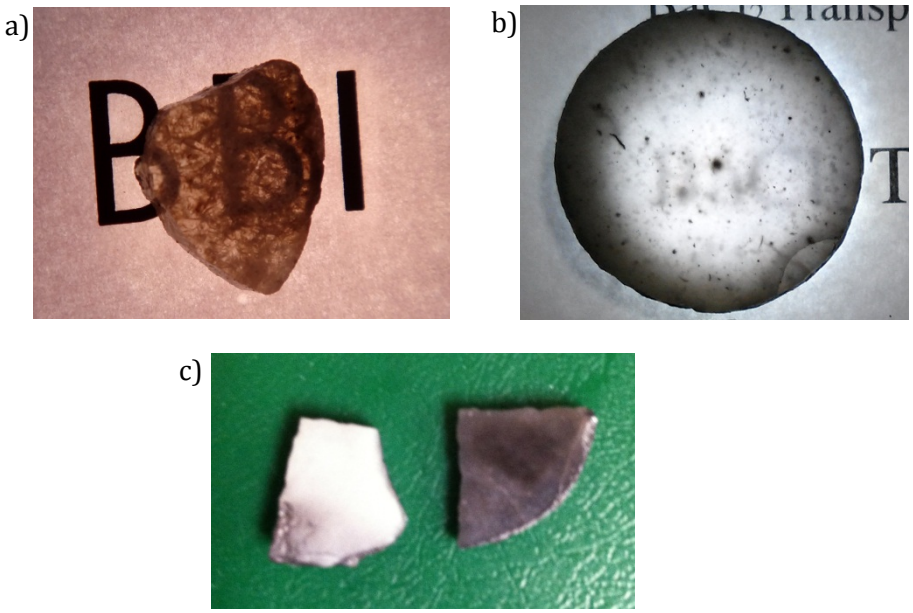

Figure 30: Backlit photographs of a 1.5mm thick 5% Eu^{2+}:BaBrI sample (a), a one inch diameter, 2mm thick backlit $BaCl_2$ sample from high purity anhydrous powder (b), and a lower purity di-hydrate $BaCl_2$ sample before and after HIPing (c)

None of the samples shown has been hot isostatically pressed. The pictures of these samples after hot isostatic pressing have not been shown, because the improvement in transparency was only marginal. In fact, the HIP seems to have introduced additional impurities due to the appearance of some milky white spots in the near-surface region of the samples.

4. CONCLUSION

The first six months of work on $BaCl_2$ and BaBrI transparent ceramics for use as gamma ray scintillators have yielded some exciting results. First of all, the sintering conditions for both compounds have been nearly optimized such that full density ceramics are achieved. The sintering mechanism of $BaCl_2$ is believed to closely follow what is expected for pure $BaCl_2$, based on the agreement in calculated activation energies for mass transport in anhydrous powders, di-hydrate powders, and resistivity data taken from the literature. More work is needed to confirm this claim by understanding the contribution of grain size and impurities/additives to the sintering behavior.

Ceramic samples of both compounds are highly colored and mildly translucent. Improvements to the handling of anhydrous BaBrI powders before hot pressing have led to significant improvements in the transparency of samples. The only processing parameters varied for $BaCl_2$ were the starting powders (di-hydrate versus anhydrous) and the pressing temperature. With only a handful of samples so far, the purity and source of the starting powder seems to have the largest effect of sample transparency. 99% purity di-hydrate powders sinter to opaque, white samples. 99.999% purity di-hydrate powders and 99.9% purity anhydrous powders sinter to translucent, brown colored ceramics. Selection of a good powder vendor for $BaCl_2$ is essential.

The structural analysis by XRD has confirmed the presence of the expected orthorhombic phase in BaBrI ceramics, but has not yet been successful in confirming the phase of $BaCl_2$ due to the difficulty in handling the hygroscopic samples. This is mainly an issue of access to an appropriate sample holder. Further analysis of the structure of $BaCl_2$ by micro-Raman spectroscopy has identified possible impurities of a mono-hydrate phase and barium oxide. The implications of the TGA results are that large amounts of water (a few weight percent) are present in even the anhydrous starting powders and it is unclear if any hydrate remains in the $BaCl_2$ or BaBrI. The

additional source of optical loss suggested by TGA is color centers at anion vacancies created by the loss of halogen gas.

Finally, the scintillation characterization of $BaCla_2$ has not yet been pursued because the early priorities include identification of impurities and color centers. On the other hand, the starting powders for BaBrI are meticulously filtered and passed through a Bridgman furnace, so europium is added. The characterization results show that the Eu^{2+}:BaBrI possesses a single x-ray excited emission line and a slightly shorter decay time than a Eu^{2+}:BaBrI single crystal. The pulse height spectrum shows no photopeak presumably because of low transparency, so the estimation of light yield and resolution are not yet possible. As processing steps are altered to eliminate impurities and defects (color centers), the study of scintillation behavior in europium doped ceramics will become a higher priority.

The immediate follow-up work to this master's thesis will include more experiments on the sintering and characterization of impurities and color centers. The first order of business is to perform thermal analysis (DTA and TGA) on all of the starting powders for both BaBrI and $BaCl_2$. This will help fill in the gaps for what impurities may be present off the shelf and what phases those impurities may evolve into during sintering. The continued use of Raman spectroscopy on the current set of samples will also help in identifying these impurities. Once the sources of impurities and color centers have been more clearly identified, appropriate alteration of the processing procedure will follow.

If continued characterization confirms that BaO is a significant impurity in BaCl2, several processing modifications are possible. First of all, ammonium chloride (NH4Cl) may be used to react with BaO impurities leaving behind BaCl2, ammonia gas, and water. A similar effect could possibly be achieved by treating the powders with hydrochloric acid before sintering. Of course the toxic nature of these exhaust gasses will need to be captured and neutralized appropriately. The final possibility for eliminating impurity and color center formation during hot pressing is reactive

atmosphere processing63. This is a technique used by the crystal growth industry to balance the vapor pressure of the halogens in order to prevent the formation of high concentrations of defects. These processing ideas will be carried out at UCF. The partnership between ORNL and LBNL should also lead to more ideas for fabricating and charactering transparent BaCl2 and BaBrI ceramics for gamma ray detection.

APPENDIX A: SAMPLE DATA

Sample ID/date	Starting Material	atmosphere	T (°C)	Time (h)	Force Schedule	notes
Barium Bromide Iodide						
1/15/2013	2012 3% Eu^{2+}	Ar_2	550	4	from RT	
1/17/2013	2012 3% Eu^{2+}	Ar_2	550	2	from RT	
1/24/2013	2012 3% Eu^{2+}	Ar_2	550 w/ degas	4	from dwell	dark gray, low translucency
1/28/2013	2012 3% Eu^{2+}	Ar_2 purge 3x	520	4	from dwell	dark gray, low translucency
1/30/2013	2012 3% Eu^{2+}	Vacuum	520	4	from dwell	lighter color, translucent
1/31/2013	2012 3% Eu^{2+}	Vacuum	520	4	from dwell	characterized at LBNL
2/5/2013	2012 3% Eu^{2+} *micronised	Vacuum	550	4	from dwell	black
4/10/2013	5% Eu new	Vacuum	580, 470	2, 6	from dwell	lighter color
4/11/2013	5% Eu new	Ar_2	580, 470	2, 6	from dwell	most homogenous, translucent
5/1/2013	5% Eu new	Vacuum, astro	580	4	from dwell	slightly darker than other vac samples
5/22/2013	LBNL purified	Vac, SPS	580	1	from RT	opaque white, fractured
Barium Chloride						
5/30/2013	99.999% purity di-hydrate	N_2	550	4	from dwell	translucent gray, ~1mm dark spots in bulk
5/31/2013	99.999% purity di-hydrate	N_2	600	10	from dwell	similar to 5/30
6/10/2013	99.999% purity di-hydrate	N_2	750	10	from dwell	better translucency, still macro-scale inhomogeneities
6/12/2013	99% purity di-hydrate	N_2	800	4	from dwell	opaque & white, HIP turns sample black
6/13/2013	99% purity di-hydrate	N_2	850	4	from dwell	opaque & white, HIP turns sample black
6/19/2013	99.9% purity anhydrous	N_2	750	10	from dwell	translucent gray, ~1mm dark spots in bulk
6/21/2013	99.9% purity anhydrous	N_2	800	10	from dwell	translucent gray, ~1mm dark spots in bulk
6/24/2013	99.9% purity anhydrous	N_2	900	2	from dwell	translucent gray, ~1mm dark spots in bulk

REFERENCES

1. Knoll, G. F. *Radiation Detection and Measurement*. 112–118 (John Wiley and Sons: 2010).

2. Lecoq, P., Annenkov, A., Gektin, A., Korzhik, M. & Pedrini, C. *Inorganic Scintillators for Detector Systems*. 243 (Springer: The Netherlands, 2006).

3. Derenzo, S., Weber, M. & Brennan, K. Scintillation Properties. at <scintillator.lbl.gov>

4. Dorenbos, P. *Scintillators for the detection of X-rays, gamma rays, and thermal neutrons*. 1–11 (Delft, The Netherlands,).at <http://www.nikhef.nl/~d90/collegediktaat/scintillators.pdf>

5. Dorenbos, P., De Haas, J. T. M. & Van Eijk, C. W. E. Non-proportionality in the scintillation response and the energy resolution obtainable with scintillation crystals. *IEEE Transactions on Nuclear Science* **42**, 2190–2202 (1995).

6. Curtarolo, S. *et al.* The high-throughput highway to computational materials design. *Nature materials* **12**, 191–201 (2013).

7. Derenzo, S. E., Moses, W. W., Cahoon, J. L., Perera, R. C. C. & Litton, J. E. Prospects for new inorganic scintillators. *IEEE Transactions on Nuclear Science* **37**, 203–208 (1990).

8. DERENZO, S. E., MOSES, W. W., WEBER, M. J. & WEST, A. C. METHODS FOR A SYSTEMATIC, COMPREHENSIVE SEARCH FOR FAST, HEAVY SCINTILLATOR MATERIALS. *Proceedings of The Material Research Society* **348**, 39–49 (1994).

9. Derenzo, S. & Bizarri, G. New Scintillators Discovered by High-Throughput Screening. *Nuclear Instruments and Methods in Physics Research A* **652**, 247–250 (2011).

10. Cherepy, N. J., Payne, S. J. & Al., E. *Scintillators with Potential to Supersede Lanthanum Bromide*. 8 (2008).

11. Setyawan, W., Gaume, R. M., Lam, S., Feigelson, R. S. & Curtarolo, S. High-throughput combinatorial database of electronic band structures for inorganic scintillator materials. *ACS combinatorial science* **13**, 382–90 (2011).

12. Singh, D. Structure and optical properties of high light output halide scintillators. *Physical Review B* **82**, 155145 (2010).

13. Coble, R. L. Transparent Alumina and Method of Preparation. (1961).

14. Petit, J., Dethare, P. & Sergent, A. Sintering of Alpha-Alumina for Highly Transparent Ceramic Applications. *Journal of the American Ceramic Society* **31**, 1957–1963 (2011).

15. Greskovich, C. & Duclos, S. CERAMIC SCINTILLATORS. *Annual Review of Materials Science* **27**, 69–88 (1997).

16. Li, Q., Zhang, G.-P., Wang, H. & Lei, L.-W. Effect of pores on transmission properties of transparent ceramics. *Optoelectronics and Advanced Materials-Rapid Communications* **5**, 673–676 (2011).

17. Seitz, F. Color Centers in Alkali Halide Crystals. *Reviews of Modern Physics* **18**, 384–408 (1946).

18. Hayes, W. & Stoneham, A. M. *Defects and Defect Processes in Nonmetallic Solids*. (John Wiley and Sons: 1985).

19. Wisniewski, D. J. & Boatner, L. A. Performance of new ceramic scintillators for gammaand x-ray detection. *Proc. of SPIE* **6706**, (2007).

20. De Haas, J. T. M. & Dorenbos, P. Advances in yield calibration of scintillators. *IEEE Transactions on Nuclear Science* **55**, 1086–1092 (2008).

21. Sakai, E. Recent Measurements on Scintillator-Photodetector Systems. *IEEE TRANSACTIONS ON NUCLEAR SCIENCE* **34**, 418–422 (1987).

22. De Mello, A. C. S. *et al.* Optical properties of pure and Cr3+ doped BGO ceramic scintillators. *physica status solidi (c)* **4**, 980–983 (2007).

23. Wang, Y. & Van Loef, E. Lu2SiO5:Ce Optical Ceramic Scintillator for PET. *IEEE TRANSACTIONS ON NUCLEAR SCIENCE* **56**, 887 (2009).

24. Van Loef, E. V. D., Dorenbos, P. & Van Eijk, C. W. E. Scintillation properties of LaCl3:Ce 3+ crystals: Fast, efficient and high-energy-resolution scintillators. *Nuclear Instruments & Methods in Physics Research Section A* **486**, 254–258 (2002).

25. Grabmaier, B. C. Crystal Scintillators. *IEEE Transactions on Nuclear Science* **31**, 372–376 (1984).

26. Cherepy, N. J. SrI2 scintillator for gamma ray spectroscopy. *Proc. of SPIE* **7449**, (2009).

27. Podowitz, S. R., Gaume, R. M., Hong, W. T., Laouar, A. & Feigelson, R. S. Fabrication and Properties of Translucent SrI2 and Eu:SrI2 Scintillator Ceramics. *IEEE Transactions on Nuclear Science* **57**, (2010).

28. Colmenares, C., Shapiro, E. G., Barry, P. E. & Prevo, C. T. A europium-doped, calcium-fluoride scintillator system for low-level tritium detection. *Nuclear Instruments and Methods* **114**, 277–289 (1974).

29. Basiev, T. T. *et al.* Fluoride optical nanoceramics. *Russian Chemical Bulletin* **57**, 877–886 (2009).

30. Rodnyi, P. A. Progress in fast scintillators. *Radiation Measurements* **33**, 605–614 (2001).

31. Laval, M. *et al.* Barium fluoride — Inorganic scintillator for subnanosecond timing. *Nuclear Instruments and Methods in Physics Research* **206**, 169–176 (1983).

32. Woody, C. L., Levy, P. W. & Kierstend, J. A. Slow Component Suppression and Radiation Damage in Doped BaF2 Crystals. *IEEE Transactions on Nuclear Science* **36**, 536–542 (1989).

33. Selling, J., Birowosuto, M. D., Dorenbos, P. & Schweizer, S. Europium-doped barium halide scintillators for x-ray and γ-ray detections. *Journal of Applied Physics* **101**, 034901 (2007).

34. Selling, J., Schweizer, S., Birowosuto, M. D. & Dorenbos, P. Cerium-doped barium halide scintillators for x-ray and γ-ray detections. *Journal of Applied Physics* **102**, 074915 (2007).

35. Yedukondalu, N. *et al.* Electronic structure, optical properties, and bonding in alkaline-earth halofluoride scintillators: BaClF, BaBrF, and BaIF. *Physical Review B* **83**, 165117 (2011).

36. Li, H. H. Refractive Index of Alkaline Earth Halides and Its Wavelength and Temperature Derivatives. *J. Phys. Chem. Ref. Data* **9**, 283 (1980).

37. Edgar, A., Bartle, M., Varoy, C., Raymond, S. & Williams, G. Structure and Scintillation Properties of Cerium-Doped Barium Chloride Ceramics: Effects of Cation and Anion Substitution. *IEEE Transactions on Nuclear Science* **57**, 1218–1222 (2010).

38. Edgar, A., Zimmermann, J., Von Seggern, H. & Varoy, C. R. Lanthanum-stabilized europium-doped cubic barium chloride: An efficient x-ray phosphor. *Journal of Applied Physics* **107**, 083516 (2010).

39. FACT salt phase diagrams. at <http://www.crct.polymtl.ca/fact/documentation/FTsalt/FTsalt_Figs.htm>

40. BLACHNIK, R., ALBERT, G. & ENNING, E. Zur Kenntnis der Zustandsdiagramme SECIJ MCI,(SE = La, Sm, Gd, Yb; M = Sr, Ba). *Z. anorg. allg. Chem.* **522**, 207–216 (1985).

41. Shannon, R. D. Revised Effective Ionic Radii and Systematic Studies of Interatomic Distances in Halides and Chalcogenides. *Acta Crystallographica* **32**, (1976).

42. Gundiah, G., Hanrahan, S. M., Hollander, F. J. & Bourret-Courchesne, E. D. Europium-doped barium bromide iodide. *Acta crystallographica. Section E, Structure reports online* **65**, i76–i77 (2009).

43. Singh, D. J. Near optical isotropy in noncubic SrI2: Density functional calculations. *Applied Physics Letters* **92**, 201908 (2008).

44. Apetz, R. & Van Bruggen, M. P. B. Transparent Alumina: A Light-Scattering Model. *J. Am. Ceram. Soc.* **86**, 480–486 (2003).

45. Bizarri, G., Bourret-Courchesne, E. D., Yan, Z. & Derenzo, S. E. Scintillation and Optical Properties of BaBrI: Eu2+ and CsBa2I5: Eu2+. *IEEE Transactions on Nuclear Science* **58**, 3403–3410 (2011).

46. Dhanaraj, G., Byrappa, K. & Prasad, V. Chapter 25.4: Pregrowth Purification. *Handbook of Crystal Growth* 851–852 (2010).

47. Osterheld, R. K. & Bloom, P. R. Dehydration Kinetics for Barium Chloride Dihydrate Single Crystals. *The Journal of Physical Chemistry* **82**, (1978).

48. Guillon, O. Effects of Applied Stress and Heating Rate in Field Assisted Sintering. *Sintering: Engineering Materials 35* 195–213 (2013).

49. Speakman, S. A. Fundamental of Rietvelt Refinement. 1–54 (2011).

50. Patterson, A. L. The Scherrer Formula for X-Ray Particle Size Determination. *Physical Review Letters* **56**, 978–982 (1939).

51. Moses, W. & Derenzo, S. E. Scintillator Characterization using the LBL Pulsed X-Ray Facility. *Radiation Measurements* **24**, 337–341 (1995).

52. Hull, S., Norberg, S., Ahmed, I., Eriksson, S. & Mohn, C. High temperature crystal structures and superionic properties of SrCl2, BrBr2, BaCl2, and BaBr2. *Journal of Solid State Chemistry* **184**, 2925–2935 (2011).

53. Lumpkin & Perlmutter Thermal and water vapor effects on the rate of the dehydration reactions of barium chloride. *Thermochemica Acta* 335–349 (1995).

54. Anthony, Bideaux, Bladh & Nichols *Handbook of Minerology Volume 1*. (2005).

55. Bhattacharya, S. Pressure-assisted densification of non-homogeneous ceramic compacts. (1997).

56. Bohley, C., Wagner, J.-M., Pfau, C., Miclea, P.-T. & Schweizer, S. Raman spectra of barium halides in orthorhombic and hexagonal symmetry: An ab initio study. *Physical Review B* **83**, (2011).

57. Herzberg, G. *Electronic Spectra and Electronic Vibration in Polyatomic Molecules*. (D. Van Nostrand Company, Inc.: New York, NY, 1966).

58. Henning, J., Beckenkamp, K. & Lutz, H. D. Single-Crystal Raman Studies on the Solid Hydrates MX2-H20 (M = Ba, Sr; X = OH, Br, I). *Applied Spectroscopy* **44**, 992–997 (1990).

59. De Waal, D., Range, K. J., Konigstein, M. & Kiefer, W. Raman Spectra of the Barium Oxide Peroxide and Strontium Oxide Peroxide Series. *Journal of Raman Spectroscopy* **29**, 109–113 (1998).

60. Kitajima, M. Defects in crystals studied by Raman scattering. *Critical Reviews in Solid State and Materials Sciences* **22**, 275–349 (2006).

61. Lenus, A. J. & Rajan, K. G. Luminescence behaviour of Eu2+-doped BaClI and BaBrI. *Materials Letters* **57**, (2002).

62. Rajan, K. G. & Lenus, A. J. X-ray excited optical luminescence studies on the system BaXY (X,Y = F, Cl, Br, I). *Pramans journal of physics* **2**, 323–338 (2005).

63. Pastor, R. C. & Pastor, A. C. Reactive Atmosphere Processing Method of Crystal Growth of Alkaline Earth Chlorides. (1978).